POLITECNICO DI TORINO

Master of Science in Electronics Engineering

Master Thesis

Development of a Miniaturized BLE-Enabled Transmitter for Wireless Charging of Active Implantable Medical Devices

Supervisors
Prof. Demarchi Danilo
Ph.D. Motto Ros Paolo
M.Sc. Del Bono Fabiana

Candidate
Toloza Hernán

Abstract

The growing trend of Active Implantable Medical Devices (AIMDs) usage is driven by notable innovations, with the integration of Wireless Power Transfer Systems (WPTS) taking center stage. These systems, marked by advancements in size reduction and enhanced power efficiency, represent a transformative force in the field of AIMDs.WPTS has transcended traditional boundaries, eliminating the need for impractical wired connections, thereby obtaining new benefits in terms of care and comfort for patients while also enhancing the convenience of patient monitoring and diagnostics for healthcare professionals.

At the core of this research domain lies the Nanochannel Delivery System (nDS), a wireless enabled Active Implantable Medical Device (AIMD) designed for drug delivery with remote control capabilities. It takes advantage of both Near Field Resonant Inductive Coupling (NRIC) for wireless power transfer Wireless Power Transfer (WPT) and Bluetooth Low Energy (BLE) for communication. Specifically, our focus centers on exploiting BLE connectivity for the wireless charging and power development of the nDS, thereby enhancing its interoperability with central devices and facilitating remote monitoring and control.

The essence of this thesis revolves around developing a Miniaturized BLE Enabled Trasmitter (TX) designed precisely for the wireless charging of nDS. It is important to note that, until now,in vivo testing has been challenging, primarily due to the reliance on a wired power supply for the TX. However, this work marks a turning point, as it enables the realization of in vivo tests. In order to achieve this, one of the main tasks is the migration of the TX into a peripheral role, enhancing the system's Internet of Things (IoT) capabilities. This shift allows us to control not just the Reciever (RX) from a central device but also our TX, simplifying the control interface and enhancing the user experience, ensuring non invasive and patient friendly healthcare.

Regarding the hardware aspect of the project, our efforts are dedicated to the miniaturization, as well as the custom board development and implementation of a Self Powering System (SPS) for the TX. The SPS enhances portability and reliability, embarking on a quest to find the ideal battery. This research includes studying diverse battery options considering different factors such as capacity,

chemical composition, maximum charge and discharge rates, and market availability. Additionally, we evaluate the efficiency of voltage regulators and the TX current requirements to guarantee a robust power supply.

In order to gauge the TX efficiency, the system was tested in different ways based on a closed-loop control closed via BLE. Different TX sizes and TX coil positions were studied in order to achieve maximum power transfer efficiency, always keeping an eye on the final packaging for device compactness. The final system under test includes commercial wireless power transfer integrated circuits: the LTC4125 fulfilled the role of the TX, while the LTC4124 roles the RX. As in previous studies, the coil with 19mm diameter for the RX has been used, delivering 30% efficiency at 6.5 mm separations between the RX and TX coils.

As regards the SPS, a prototype has been tested, featuring a Buck Converter (TPS82740) generating a 3V output for the TX's microcontroller (MCU) and a Boost Converter (TPS61023) with a 5V output for the LTC4125. Powering the SPS, a 3.7V Polymer Li ion battery with a capacity of 2000 mAh was selected (SR674361P), ensuring the necessary support for nDS battery charging.

Acknowledgements

A mi madre, Daniela, y a mi padre, Pablo. A mis hermanas, Ariana, Fiama y Tais. A toda mi familia y amigos, que gracias a su apoyo incondicional hicieron posible este trabajo. A todas las personas que me han brindado la oportunidad de estar aquí hoy. Gracias.

Contents

List of Tables

List of Figures

Acronyms

AIMDs Active Implantable Medical Devices

WPTS Wireless Power Transfer Systems

WPT Wireless Power Transfer

nDS Nanochannel Delivery System

AIMD Active Implantable Medical Device

NRIC Near Field Resonant Inductive Coupling

BLE Bluetooth Low Energy

IoT Internet of Things

SPS Self Powering System

TX Trasmitter

RX Reciever

PCB Printed Circuit Board

DAC Digital to Analog Converter

MCU Microcontroller Unit

NCC Near-Field Capacitive Coupling

SAR Specific Absorption Rate

PTE Power Transfer Efficiency

EMF Electromotive Force

GAP Generic Access Profile

ATT Attribute Protocol

GATT Generic Attribute Profile

PHY Physical Layer

Li-Ion Lithium-Ion

Li-Po Polymer Lithium-Ion

SPI Serial Peripheral Interface

NTC Negative Temperature Coefficient

Chapter 1

Introduction

The Wireless Power Transfer (WPT) technique has long been regarded as an optimal technical solution for powering electric-driven devices, dating back to the 1910s when Nikola Tesla introduced his ideas, and at present particularly gaining prominence in the context of Active Implantable Medical Devices (AIMDs). In this regard, WPT technologies play a crucial role in addressing two major issues associated with battery-powered devices like AIMDs: firstly, the challenge of short battery life, and secondly, the issue of high initial costs [1]. By leveraging the WPT technique, AIMDs can efficiently tap into wireless power from the surrounding electromagnetic field, allowing them to charge their batteries seamlessly, even while in motion. Amongst various WPT techniques, Near-field Resonant Inductive Coupling (NRIC) is considered the most efficient method for energizing AIMDs,fulfilling their energy needs without causing harm to the adjacent tissue [2].On the other hand, but equally relevant, communication with AIMDs plays a crucial role, especially when the measurement of specific parameters and the issuance of instructions for its control are necessary. At this juncture, the Bluetooth Low Energy (BLE) protocol comes into play, enabling the establishment of bidirectional and stable communication between a master, also referred to as a central unit, and a slave node, also known as a peripheral. Following the precedent set by previous works, which also involved the use of AIMDs [3], BLE is selected for its capability to facilitate wireless communication, driven by its advantageous features of low power consumption and efficient data communication speed. The central aim of this work is to develop a miniaturized BLE Enabled Transmitter(TX) designed precisely for the wireless charging of a Nanochannel Delivery System (nDS), a wireless enabled AIMD designed for drug delivery with remote control features [4]. This dissertation presents the execution of the Wireless Power Transfer (WPT) system, BLE communication, as well as the Transmitter (TX) system, and outlines the objectives of this investigation.

Chapter 2 encompasses the state-of-the-art overview for this thesis, spanning essential knowledge of WPT systems and Bluetooth Low Energy, detailing the LTC4125 transmitter, and delving into the examination of various elements comprising a powering system (including battery analysis and voltage regulators). The chapter concludes with an analysis of an established closed-loop WPT system.

Chapter 3 delineates the design of two distinct versions of the TX board, incorporating various considerations and modifications.

Chapter 4 elucidates the comprehensive design of the self-powering system board, encompassing battery and voltage regulator selections, culminating in the final Printed Circuit Board (PCB) design.

Chapter 5 explores the migration of the TX from a central to a peripheral role, considering the primary activities the transmitter will perform and the key parameters to be addressed.

Chapter 6 presents the tests and results obtained with different TX board designs and system configurations. Firstly, the TX boards were tested with the TX in a central role, employing various coil arrangements, and secondly, with the TX in a peripheral role.

Chapter 7 offers conclusions and outlines the prospects on the horizon.

Chapter 2

State of Art

2.1 Overview of Active Implantable Medical Devices

In recent years, there has been a noteworthy transformation in implantable electronic devices evolving into invaluable biomedical tools. From here, the currently thriving Active Implantable Medical Devices (AIMDs) originate, playing a crucial role in monitoring, measuring, and eliciting physiological responses in vivo through the use of wireless communication [5]. Lately,dedicated healthcare professionals have invested their endeavors to enhance the well-being of patients through diverse AIMDs, including cochlear implant, wireless pressure sensor implant, the implantable cardiac defibrillator, and implanted bladder stimulator [6]. In the domain of the most recent AIMDs, the trend is towards minimizing dimensions and energy consumption while enhancing therapeutic effectiveness and safety,resulting in devices capable of direct implantation onto the targeted organ.In this perspective, this research exploits a compact Nanochannel Delivery System (nDS) designed to fulfill the need for tailored therapy, aiming to achieve optimal treatment efficacy with minimal side effects [4].

2.1.1 Nanochannel Delivery System

nDS is designed to deliver controlled drug doses to patients managing chronic conditions that need continuous therapeutic intervention. Constructed with silicon nanofluidic material, the nDS incorporates a membrane where the surface charge impacts the density of ionized particles within its nanochannels. Employing voltage between the cellular membrane and the electrolytic mixture enables precise control over surface charge and nanochannel charge selectivity [7], [4].This device encompasses a drug reservoir and a Printed Circuit Board (PCB) responsible for system control. The PCB includes:

- The CC2640R2F for the control
- A Digital Temperature Detector
- A Circuit for Managing Membrane Voltage (exploiting the MAX5532 a Digital to Analog Converter (DAC))
- A 2.4 Gigahertz Antenna

Remote control of the nDS is facilitated through the use of the Bluetooth Low Energy (BLE) protocol, operated by the Microcontroller Unit (MCU), while for powering the device it make use of the LIR2025 (RS PRO) battery with a capacity of 25 mAh [8]. Refer to Figure 2.1 for a visual representation of the nDS device:

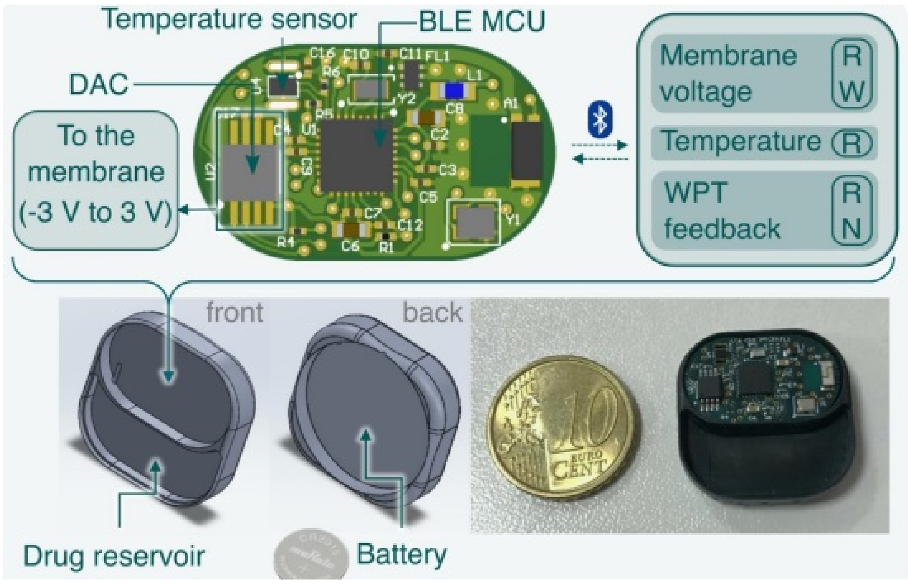

Figure 2.1: Nanochannel Delivery System Device [7]

2.2 Wireless Power Transfer

The breakthrough made by Michael Faraday in 1831, uncovering electromagnetic induction, facilitated the transfer of electrical energy between coils without requiring a conductive medium. This breakthrough led to the development of transformers, the inaugural devices capable of power transfer without dedicated delivery circuits. Despite their innovation, the primary limitation was the requirement for robust coupling, constraining the permissible separation between the coils [9]. At the outset of the 19th century,the concept of transmitting power across substantial distances emerged later, with Hertz and Tesla proposing this idea . While Tesla concentrated on resonance and its application in efficient wireless power transfer, Hertz conducted the first-ever WPT experiment, primarily aimed at validating the existence of electromagnetic waves. Following this experiment, Hertz successfully demonstrated the feasibility of transmitting power without a direct connection [10].

WPT systems have evolved into increasingly viable solutions for energizing sophisticated devices, including biomedical implants such as pacemakers and defibrillators [11], as well as neurostimulators and drug delivery systems [12]. With the rapid advancement of technology in recent decades, numerous methodologies have been proposed for wirelessly powering these implanted devices. Among these, near-field capacitive coupling, near-field inductive coupling, and ultrasonics stand out as diverse strategies for empowering implantable devices [13].

The diagram depicted in Figure 2.2 illustrates the configuration of the Near-Field Capacitive Coupling (NCC) technique. Enabling wireless energy transfer through the tissue layer, the NCC functions derived from the idea of coupling electric fields amongst two set of conductive arrays, each expressly dedicated to the pathways of forward and reverse current. The removal of the necessity for physical contact is accomplished through the displacement current present between these conductors. The NCC approach operates at a high frequency (in the range of several tens of megahertz) to ensure efficient power transmission. Consequently, tissue losses, become significant in the NCC link. These losses must be assessed using optimization models, as they constitute the primary contributors to overall losses. A crucial design objective for enhancing the power handling capacity of the NCC link is to minimize tissue losses and, consequently, the Specific Absorption Rate (SAR).

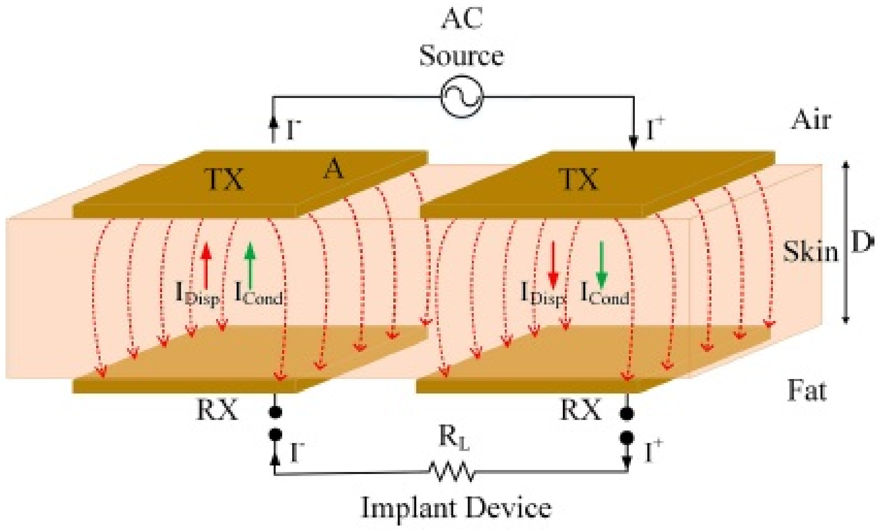

Figure 2.2: Schematic of the NCC method [13]

Concerning Ultrasonic Energy Transfer, this method utilizes propagating ultrasound waves with frequencies exceeding 20 kHz to transmit energy wirelessly. Unlike electromagnetic approaches that possesses the ability to convey energy in a vacuum, ultrasonic energy transfer requires a medium, though not necessarily a conductive one, for propagation[13]. In the realm of embeddable applications, the conveyance of energy to an implanted device is made possible by ultrasound waves passing through tissues, where a piezoelectric transducer converts it into electrical energy. Figure 2.3 illustrates a typical ultrasonic energy transfer system. The Power Transfer Efficiency (PTE)) stands as the primary metric for assessing the effectiveness of a wireless connection and is quantified as the ratio of power delivered to the load (the implant, in this instance) to the power drawn from the source (the transmitter).A noteworthy constraint of this technique is the non-uniformity of acoustic resistance in the human body, which confines device placement to soft tissues with low acoustic impedance.

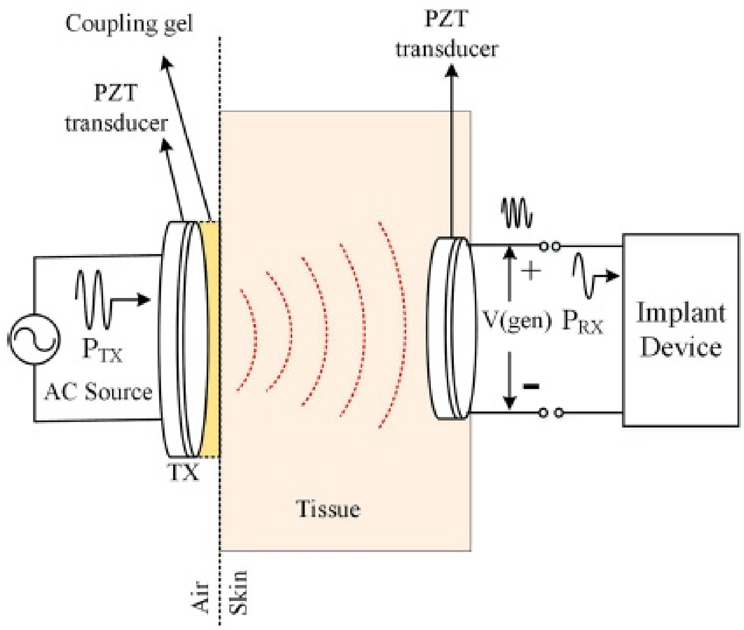

Figure 2.3: Schematic of the ultrasonic energy transfer method [13]

The chosen method for implementation in our Wireless Power Transfer (WPT) system is Near-Field Resonant Inductive Coupling (NRIC) and functions under the principle of electromagnetic induction. In this scheme, a time-varying magnetic field is generated by a transmitting coil placed close to the skin, causing the induction of an Electromotive Force (EMF) in the receiving coil located inside the body, as illustrated in Figure 2.4.

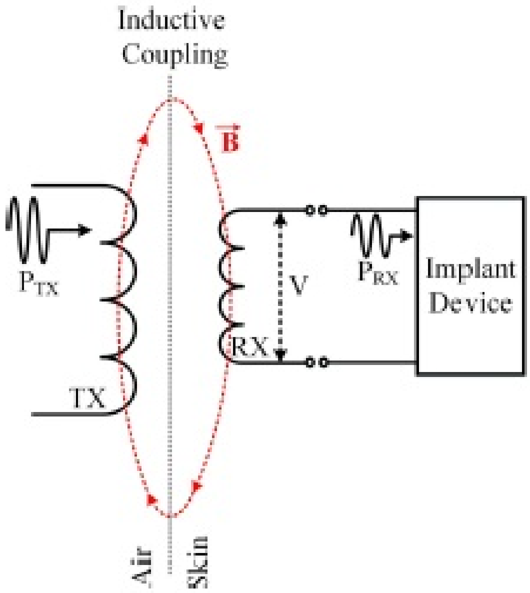

Figure 2.4: Illustration of the NRIC power transfer method [13]

The proximity of the transmitter (TX) and receiver (RX) coils results in a loose coupling, where less than ten percent of the magnetic field generated by the transmitter effectively contributes to inducing electromotive force (EMF) at the receiver. As a consequence, optimizing the power transfer efficiency of the system becomes paramount. In an implanted setting, the design of the link is bound by application specifications, including the separation between TX and RX, dimensions of the RX, and the operational frequency.

In NRIC links, the frequency of operation is restricted to a few tens of MHz, where coil losses outweigh tissue losses (due to induced currents) in this range. Therefore, the selection of excitation frequency and strength is crucial for generating a sufficiently large EMF for the intended implant application. The resulting electromotive force (EMF) is intricately linked to both the intensity of the transmitting (TX) current and the operational frequency. However, constraints arise from the necessity to adhere to the maximum permissible field strength for safe tissue operation, coupled with considerable tissue attenuation at elevated frequencies This makes it noteworthy that the frequency of operation is chosen to minimize implant coil losses, rendering it suitable for AIMDs.

2.3 Bluetooth Low Energy

Bluetooth Low Energy (BLE) stands out as an advancing low-energy wireless technology tailored for controlling and monitoring over short distances. It embodies a balance between energy efficiency and latency, providing a single-hop solution suitable for diverse applications in healthcare, consumer electronics, smart energy, and security [14]. Leveraging its distinctive traits, encompassing moderate power consumption and swift data communication, BLE is the chosen technology for establishing communication with our device.

2.3.1 BLE Structure

The Bluetooth LE stack comprises multiple layers and functional modules, with some being obligatory and others optional [15]. The structure of BLE can be segmented into three distinct blocks [16], as depicted in Figure 2.5:

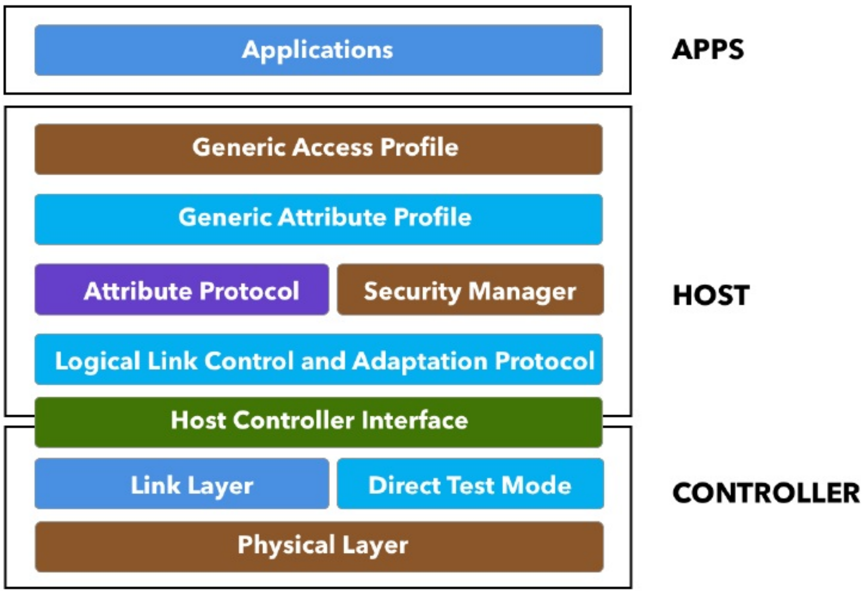

Figure 2.5: Structure of BLE [16]

For our specific application, our focus will be on the upper-level layers, specifically the APPLICATION block and the HOST block. As for the CONTROL layer, we will delve into key concepts to grasp the functioning of the system.

2.3.1.1 Application

Essentially, the application layer pertains to how the application manages the data it receives from and sends to other devices, along with the underlying logic. This layer is the interface through which we can interact with the device to impose, read, and modify various parameters based on the specific application. It concerns the deployment built on the Generic Access Profile and Generic Attribute Profile. In Chapter 5, we will delve into this section more comprehensively, elucidating the implemented changes for the functioning of our device in accordance with its requirements.

2.3.1.2 Host

The host section comprises several layers, each offering alternative implementations of Bluetooth mesh protocols and procedures. Notably, the most relevant layers for our application are listed below:

- Generic Access Profile
- Attribute Protocol
- Generic Attribute Profile

2.3.1.2.1 GAP: Outlines advanced data categories, defining services, characteristics, and descriptors in relation to the foundational attributes found in the attribute table. At the heart of GAP's operations lies the pivotal process of transmitting advertising packets (advertising) and their reception through scanning.

2.3.1.2.2 ATT: Guides the manner in which a server showcases its organizational framework to a client Within ATT, two distinct roles come into play: the server and the client [16]. In the server role, a device discloses the data it manages, accepting commands and responding with notifications and indications. The server's exposed data is organized as attributes, wherein an attribute defines a specific data type revealed by the server and outlines its structure. Services and characteristics, exemplified later, are prime instances of attributes. Attributes consist of:

- Attribute type (Universally Unique Identifier or UUID): 16-bit or 128-bit number, depending on whether it is a Bluetooth SIG-Adopted Attribute or a custom attribute type created by the developer.
- Attribute Handle: Assign by the server. Simply, is 16-bit value assigns it to each attribute, akin to an address. The client utilizes this value to reference

a particular attribute, with the server ensuring its uniqueness throughout the connection between two devices.

- Attribute Permissions: Authorization dictates whether an attribute is1 accessible for reading or writing, capable of notification or indication, and the mandated security thresholds for such actions. These authorizations are established at an elevated stratum, either the GATT layer or the Application layer.

The visual representation below offers a logical depiction of an attribute:

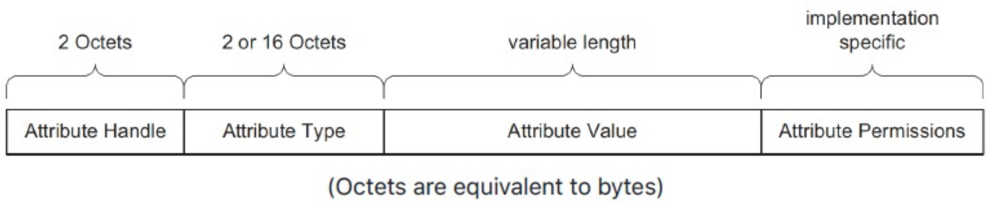

Figure 2.6: Attribute Representation [16]

On the client side, it interfaces with the server to read the exposed data and control the server's behavior. This involves sending commands, requests, and acknowledging incoming notifications and indications.

2.3.1.2.3 Generic Attribute Profile: The Generic Attribute Profile (GATT) delineates modes of operation and procedures applicable in a non-connected state, addressing aspects like leveraging advertising for connection-less communication and executing device discovery. Additionally, GATT specifies security levels, modes, and certain user interface standards [15]. Within GATT, the delineation of the services and their characteristics is defined. Services and characteristics represent distinct categories of attributes, each serving a specific purpose. Services and characteristics will be elaborated upon in detail later.

2.3.1.3 Controller

As illustrated in Figure 2.5, this segment primarily comprises the Physical Layer (PHY) and the link layer. Concerning the PHY, it encompasses all aspects of Bluetooth technology related to radio frequency (RF) utilization, encompassing modulation schemes, frequency bands, channel allocation, and characteristics of transmitters and receivers.

Remarkably, BLE functions within the 2.4 GHz spectrum, specifically the ISM band, partitioned into 40 RF channels with a 2 MHz separation. Within this framework, three channels are assigned as Primary Advertising Channels, while the remaining 37 channels facilitate Secondary Advertisements and data transmission during a connection [16]. Conversely, the link layer interacts with the physical layer, providing abstraction and a mode of interaction for higher-level layers. This layer, is also responsible of the management of the different states of the physical layer, where the three main states of operation are: advertising, scanning and connected state. Figure 2.7 illustrates the different link layer states:

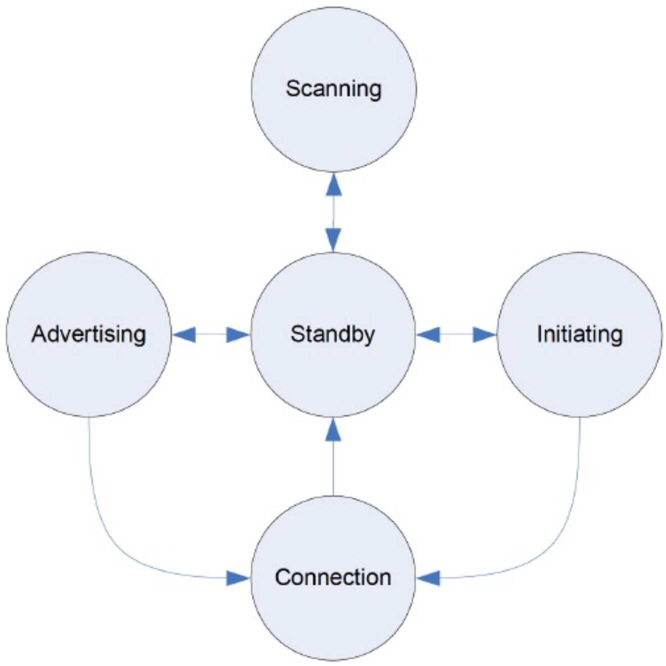

Figure 2.7: Link Layer States [16]

The primary states in BLE operation are the advertising and scanning states. When a device is in the advertising state, it permits other scanning devices to detect and potentially establish a connection with it. If the device under the role of advertising is open to connections and a device that is in that moment scanning locates it and opts to link, both devices transition into the connected state, facilitating data exchange. A more detailed explanation of this process will be provided in the subsequent sections. As for the initiating state, it occurs when a scanning device decides to initiate a connection with an advertising device. On the other hand, the standby state is the default condition in which the physical layer remains inactive, neither transmitting nor receiving data.

2.3.2 BLE devices: The Central and Peripheral Roles

Our focus will be directed towards the examination of the pivotal device roles, particularly defined during a connection state: these roles encompass the peripheral and central roles. When a device initiates a connection, progressing from the Initiating state to the Connection state, it takes on the Central role. Conversely, when a device acknowledges a connection request, moving from the Advertising state to the Connection state, it assumes the Peripheral role.

These roles find their definition in the link layer, while the peripheral and central roles are explicitly outlined in the GAP layer. The exploration and comprehension of these two roles are paramount, as one of the primary objectives of our study involves transitioning our device from a central to a peripheral role.

2.3.3 Advertising and Scanning

For two BLE devices to establish communication, one device must broadcast its presence, while the other scanning to identify advertisement packets from the broadcasting device, and then been able to start a connection. Our attention will be directed toward understanding these fundamental states.

2.3.3.1 Advertising State

In this phase, a device dispatches packets that carry essential information intended for reception and interpretation by other devices. These packets adhere to a predefined timetable referred to as the advertising interval. The initiation of advertising consistently starts with the transmission of packets across the trio of Primary Advertising Channels, wherein the advertisement data is confined to 31 bytes. This process enables central devices to recognize and decode the advertising device (peripheral) along with its advertisement packets. Following this, the central device can commence a connection if granted permission by the advertising device. Moreover, the central has the option to request a scan request. If the advertiser supports this feature, it responds with a scan response. Scan requests and responses enable the advertiser to transmit supplementary advertising data that couldn't be accommodated in the initial advertisement packet.

2.3.3.2 Scanning State

Centrals systematically synchronize themselves with the trio of Primary Advertising Channels. As a result, for a central device to identify a peripheral, it needs to be tuned to the exact channel on which the peripheral is actively advertising at that particular time. An active scanning mode refers to a device involved in actively listening for advertisements and subsequently dispatching scan requests to the advertisers. On the contrary, a passive scanning mode characterizes a device that passively observes advertising packets without initiating scan requests. The primary scanning parameters are illustrated in Figure 2.8:

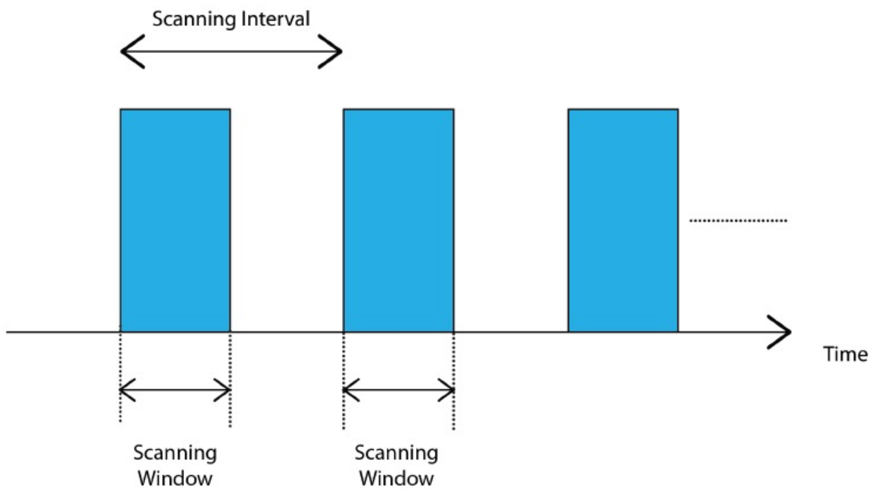

Figure 2.8: Scanning parameters [16]

The device actively listens for the entire scan window during each scan interval, tuning in to a different Primary Advertising Channel in each scan window.

2.3.4 Services and Characteristics

The exploration and utilization of Services and Characteristics will be a focal point for the functionality of our device, and the reasons for this emphasis will be outlined later.

A GATT service is thoroughly defined by a service specification, providing a detailed outline of its characteristics and descriptors. The expected responses of the GATT server, which hosts the service, to various conditions and state data values, are precisely detailed within this service specification. Furthermore, a service encompasses additional attributes, distinct from characteristics, which contribute to the organization of data within the service. These attributes may include service declarations, characteristic declarations, and others.

In the context of a service, a characteristic plays a vital role, representing a specific information the server intends to show to a client. As an illustration, the battery level characteristic indicates the remaining power level of a device's battery, accessible to a client. The characteristic is accompanied by other attributes:

- Properties: Characterized by a predefined set of bits, outlining the permissible ways in which a characteristic value can be employed. Illustrative examples encompass the capacity for reading, writing, writing without a response, notification, and indication.

- Descriptors: These elements house supplementary information related to the characteristic value.

Figure 2.9 illustrates the visual representation of various services with their respective characteristics:

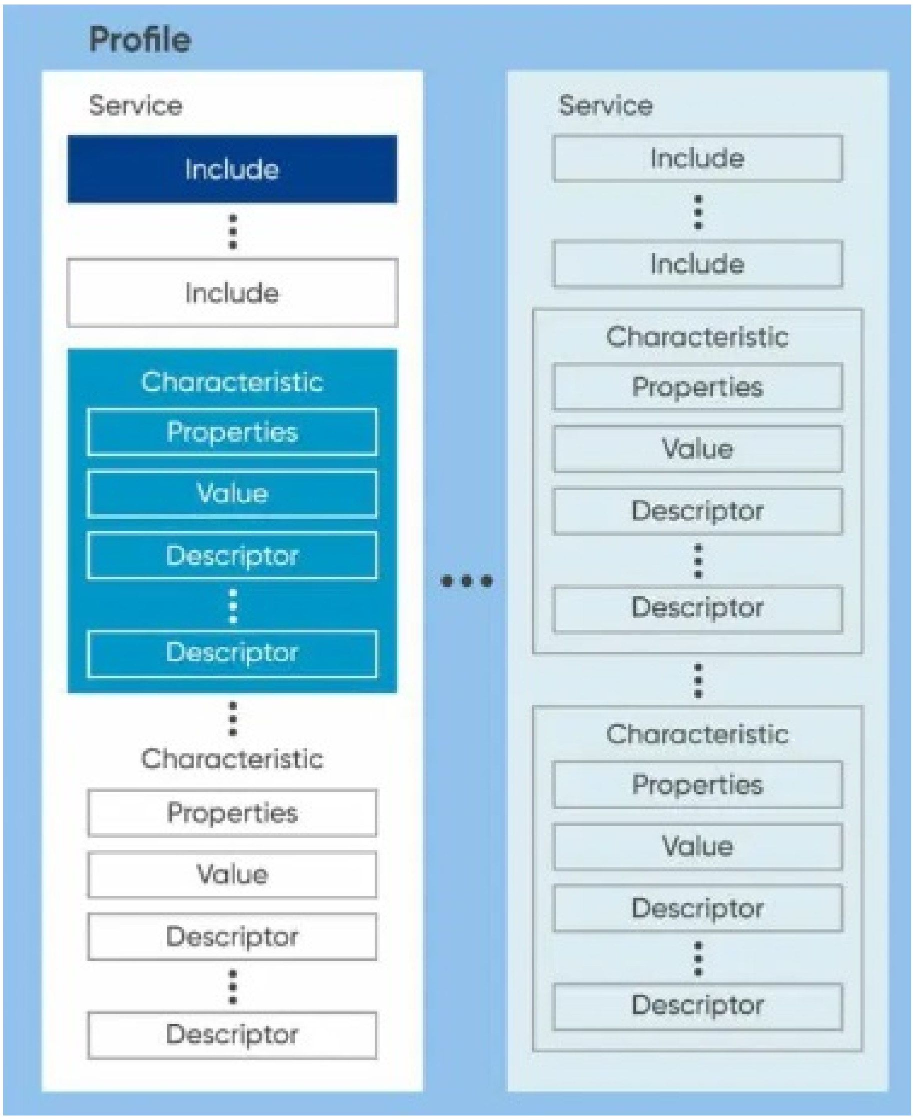

Figure 2.9: Services and Characteristics[17]

An example showcasing the utilization of a service, as implemented in [17], is presented subsequently. This example pertains to the Heart Rate Service (HRS), designed to relay heart rate information to a monitoring device.

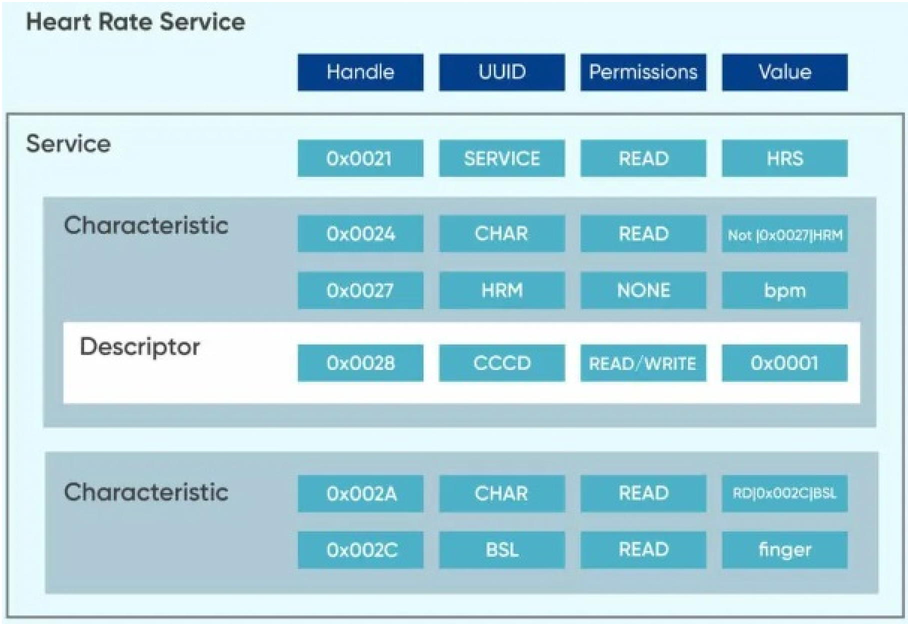

Figure 2.10: Heart Rate Service [17]

2.3.5 Transition from Central to Peripheral Role

Currently, our TX device operates in central mode, while the RX serves as a peripheral. This setup allows our peripheral device to alert the TX through periodic notifications. The TX, in turn, waits for new directives to make decisions regarding the transmitted power value [7]. Chapter 5 provides a detailed explanation of this process and the variables involved. However, when it comes to real-time data collection, this system is not practical as it requires physical manipulation of the devices, making it impractical for in-vivo tests. This is the motivation behind changing the role of the TX.

Switching the TX from a central role to a peripheral one involves introducing a third device into the system to serve as the central role. This device will be responsible for the control and manipulation of both the RX and the TX. In this way, we leverage the services and characteristics of BLE to facilitate communication between devices, enabling safe, efficient, and practical in-vivo testing.

2.4 Transmitter LTC4125

The LTC4125 plays a pivotal role in our system, serving as the primary component for wireless power transmission control [18] between itself and the properly tuned RX. Essentially, it fine-tunes its driving frequency to align with the LC network's resonant frequency, thereby regulating the current flow through it and, in turn, delivering power to the tuned receiver. To enhance transmission efficiency, the LTC4125 offers various features while also halting power delivery under specific circumstances.Between these main attributes we can find:

- Auto-Resonant function
- Optimum Power Search
- Foreign Object Detection

The LTC4125 functional block diagram is shown in Figure 2.11:

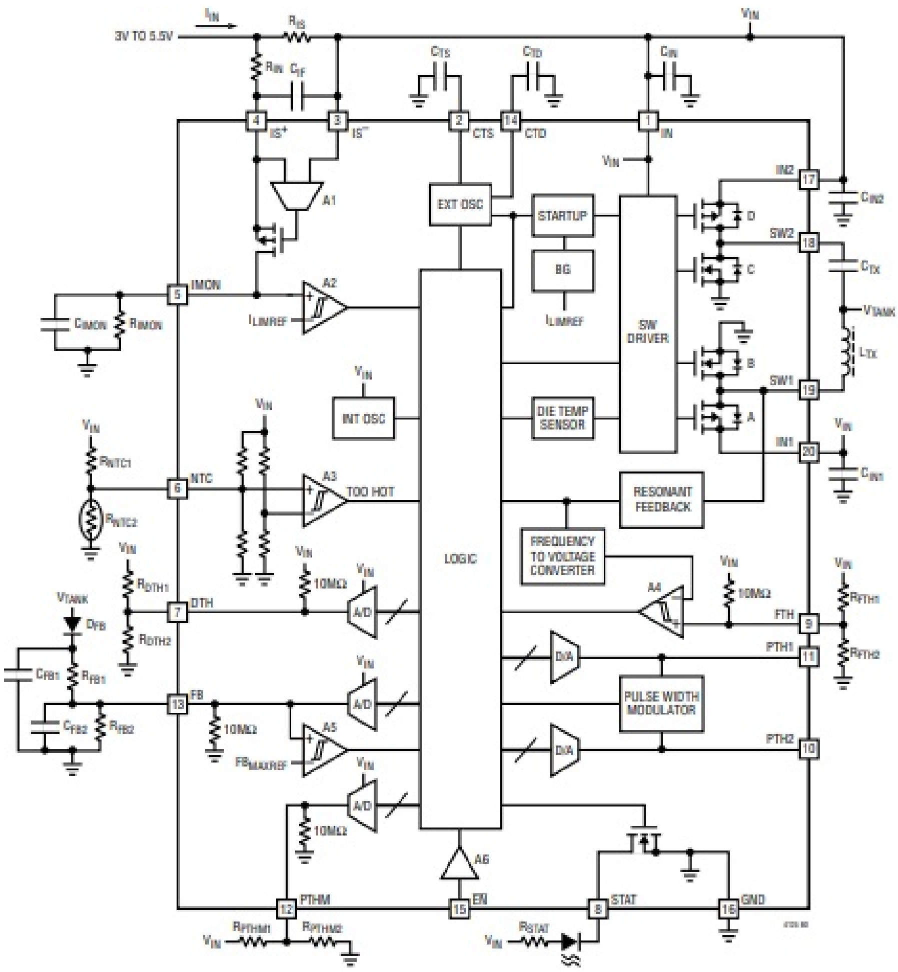

Figure 2.11: LTC4125 Functional Block Diagram [18]

2.4.1 Auto-Resonant function

The Auto Resonant function of the LTC4125 plays a crucial role in maximizing available receiver power. It achieves this by adjusting the drive voltage frequency in the LC TANK based on the detected current passing through it. This functionality ensures that the current and voltage at the SW pins remain in phase, thereby maintaining resonance frequency in the LC network. This feature is essential for the WPTS to attain its highest Power Transfer Efficiency. In Figure 2.12, the LC tank voltage waveform is depicted in red, the LC tank current waveform in green, and the input wave at the resonant frequency in blue.

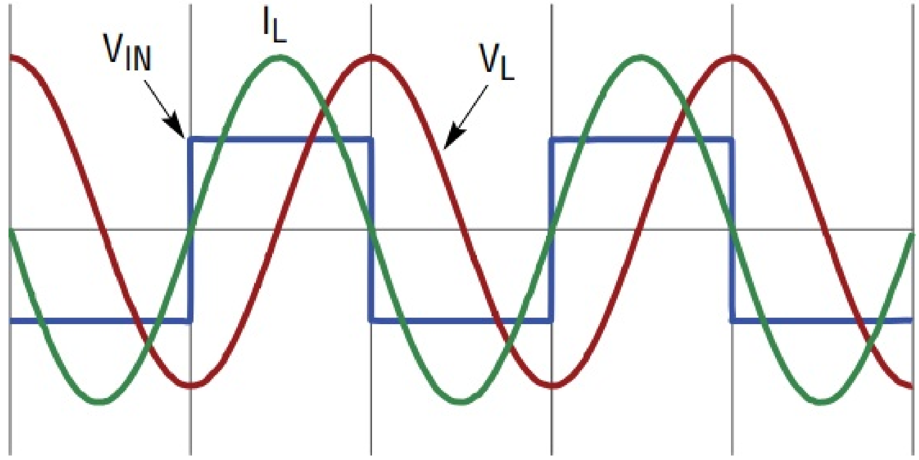

Figure 2.12: Voltage and Current Waveforms at the resonant frequency [18]

2.4.2 Optimum Power Search

This algorithm operates by manipulating the pulse width of the full-bridge driver situated on the SW pins. Its primary aim is to alter the power of the magnetic field produced by the transmit coil, ensuring adequate power is supplied to sustain the load at the receive coil. The proportional relationship between the LC tank current and voltage to the pulse width means that by adjusting the pulse width, we gain control over the intensity of the magnetic field.

Figure 2.13 shows how the algorithm is segment into three different phases: T1, T2 and T3. In the first phase (T1), given a certain voltage from the PTHM pin, the device transmit a constant power value.Then, in order to detect a valid RX, and though a pulse width modulation (PWM) by the driver of the full bridge, a gradual increase (through incremental steps) in the transmitted power is apply during a second phase (T2). If the presence of a RX is detected, the next phase starts (T3), remaining constant the power transmitted.Otherwise, the step-wise linear ramp is increased until it reaches its limit and by now the transmitted power descends to zero, going back to the starting point (T1).

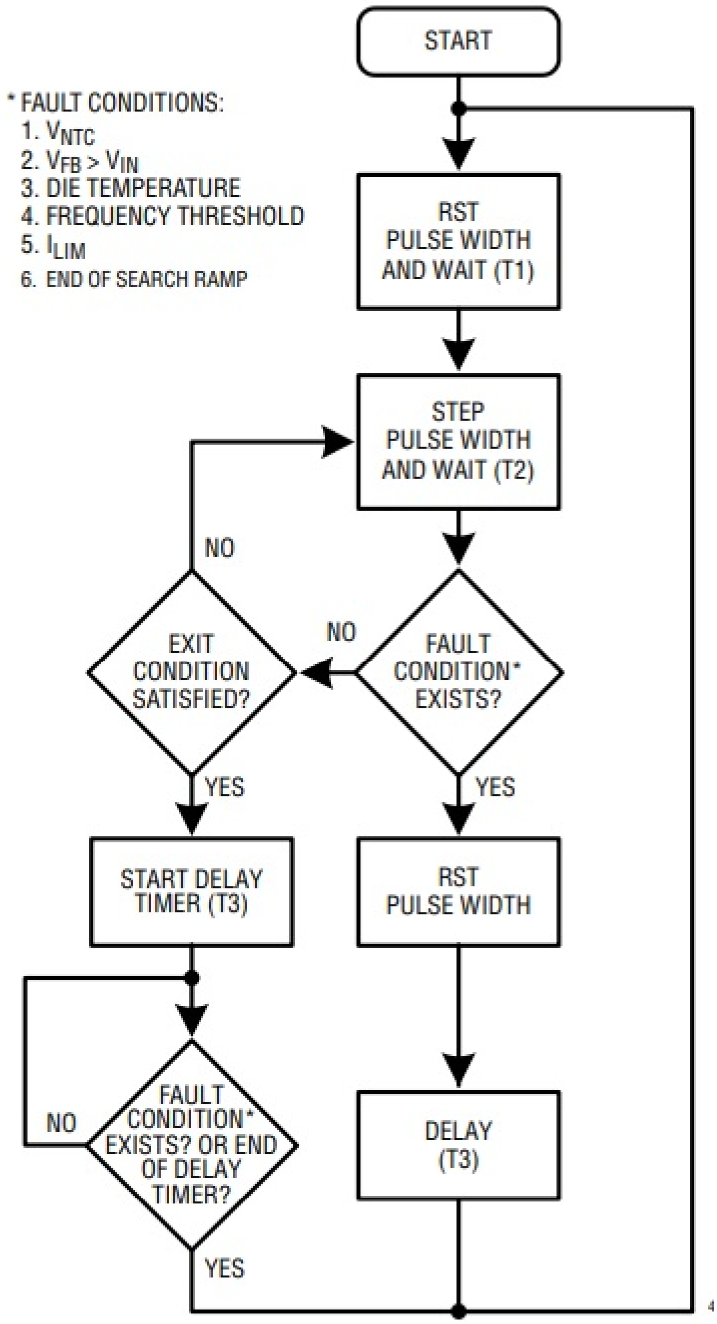

Figure 2.13: Algorithm Flow Chart [18]

2.4.2.1 Fault Conditions

As we mention before, the LTC4125 halts power delivery under specific circumstances during the Optimum Power Search, implementing six different fault conditions [18] :

FAULT CONDITION	DETECTION BY
Excessive temperature of the coil	NTC pin
Excessive tank voltage	FB pin
Foreign Object Detection	Frequency from the FTH pin
Input current limit I_{LIM}	IMON pin
End of search ramp	
Internal (die) over temperature	

Table 2.1: LTC4125 Fault Conditions

In the event of these error conditions enumerated in Table 2.1, the STAT pin goes into high impedance to signal the absence of power being supplied to the RX coil. The input current limit I_{LIM} is the only exception from which the STAT pin does not go to high impedance.

2.4.2.2 Exit Conditions

In order to guarantee that the proper optimum transmit power is reached,thereby identify a valid RX, the LTC4125 employs different exit conditions during the second phase and can be divided in primary and secondary exit conditions. Regarding the first ones, these are not user programmable and works under the evaluation of the maximum LC tank voltage detected by the FB pin,ending the exploration as soon as the LTC125 finds a meaningful difference in the LC tank. On the other hand the secondary exit conditions are:

- Input Current Threshold
- Differential Tank Voltage Threshold

The Input Current Threshold I_{TH} can be set by using R_{IN}, R_{IMON}, and R_{IS} [18]:

$$I_{TH} = \frac{R_{IN}}{R_{IMON}} * \frac{0.8V}{R_{IS}} \tag{2.1}$$

Where, $V_{ITH,typ} = 0.8V$. Looking at Figure 2.11 we have that:

- V_{IMON} : Differential voltage across R_{IS}

When $V_{IMON} > 0.8V$ the I_{TH} is reached. so the search will stop and the pulse amplitude is maintain until the following search period.

Regarding the Differential Tank Voltage Threshold, it exploits the DTH pin to set a voltage threshold on the FB pin. Then, a comparison in made between this threshold and the FB pin voltage increase;the exit condition is met if the threshold is exceeded. This exit condition is useful in presence of poor coupling between the TX and the RX.

2.4.3 Temperature Monitoring

Continuous monitoring of the transmit (TX) coil temperature is essential for ensuring safe operations and preventing overheating. The LTC4125 incorporates the over-temperature fault as a crucial condition within the Optimum Power Search method. To establish the temperature fault threshold, it is necessary to connect a Negative Temperature Coefficient (NTC) thermistor amongst its corresponding pin and the ground pin [18]. In a standard configuration, the LTC4125 identifies a fault condition when the resistance of the NTC thermistor drops to 0.538 times its value at 25°C, corresponding to 41.5°C. Power transmission is suspended if the coil temperature exceeds this threshold, resuming only when the temperature decreases to a safe level.

In the context of the evaluation kit DC2770A from Analog Devices, used as a reference according to [19], it implements the MURATA FTN55XH103FD4B thermistor. This thermistor has a 10Kohm resistance at 25°C and is strategically placed beneath the coil to measure the post-critical temperature for the circuit [20] .

2.4.4 Prior Work Insights

In the context of [7], [21], a significant issue became apparent regarding the accuracy of the primary exit condition in the TX's open-loop control. Open-loop, in this context, signifies the absence of a feedback mechanism between the TX and RX within the system. This lack of feedback was found to be a critical factor contributing to the aforementioned issue.

To address this challenge, a proposed solution was introduced, involving the implementation of a closed-loop network designed to sidestep the FB pin, since the reliance of the TX on the V_{FB} signal to ascertain the existence of the receiver while the Optimum Power Search phase. Within this refined system configuration, the RX provides real-time feedback to the TX, enabling dynamic adjustments to the transmitted power through a straightforward voltage modification on the PTH pin.

To design the TX board, various modifications of the evaluation kit DC2770A were considered. These modifications ranged from altering the IMON pin [7], [21] to adjusting the PTHM and PTH pins circuit [7], [22].

2.4.4.1 IMON pin Modifications

The first adjustment involves fixing the IMON pin voltage to a higher value [7], [21] compared to V_{ITH}, previously explained in 2.4.2.2 [18]. This is obtained by the implementation of a voltage divider between the power supply and ground. This modification is intended to compel the algorithm to promptly identify a valid RX right after phase T2, thus progressing to the subsequent phase, T3. Figure 2.14 illustrates the PTH voltage before and after this modification, demonstrating how the second phase is effectively canceled out.

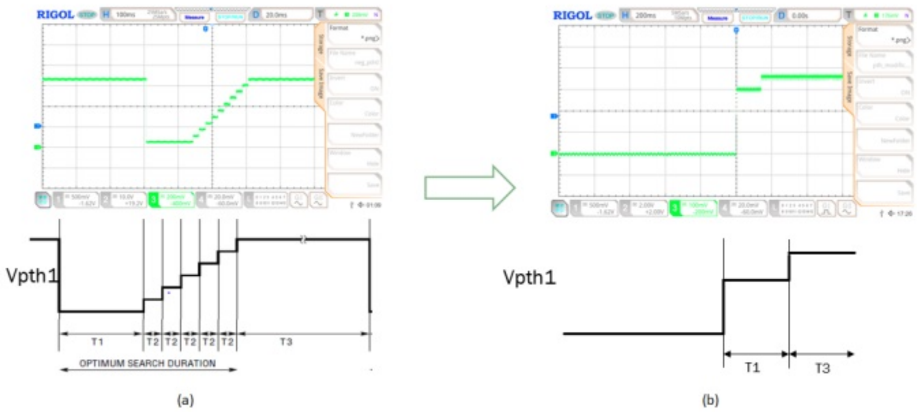

Figure 2.14: PTH voltage before (a) and after(b) the IMON modification [21]

2.4.4.2 PTH and PTHM Control System

In this case, several modifications were implemented. Initially, a power control circuit was designed for the transmitter, incorporating the use of the PTH pin, along with a modification to the PTHM pin [21]. Subsequently, to ensure the reliability of recharge cycles when using different RX coils and to ensure higher power transmission, a second adjustment was made in the PTH circuit [22].

To start with, we know that in the evaluation board [19], the PTHM pin is connected to ground, so then the PTH pin has a minimum initial value in phase T1. The first adjustment is then, though the voltage divider in PTHM pin, set the PTHM pin to a higher value in phase T1, obtaining with this an improvement in the efficiency of the system.

The next modification involves the PTH pin, that, despite is not being conventionally designated as an input pin, it was repurposed as such to influence the modulation of the LC tank control signal. To achieve it, an N-Channel MOSFET (TN0702 from Microchip) in series with a resistor were employed to manage the charging and discharging of a capacitor linked by PTH pin. The manipulation of the N-MOSFET's state, controlled by a specific signal, allows for the adjustment of the capacitor voltage at the PTH pin, thereby governing power transmission.

Integrated for precise control of the N-MOSFET, a feedback loop comprises a Digital to Analog Converter and a comparator (by means of the MAX5532EUA and the TLV7011 respectively). This mechanism evaluates the capacitor voltage against the DAC-defined threshold. When the voltage on the condenser surpasses the up limit, the comparator output goes high, saturating the gate of the N-MOSFET and enabling capacitor discharge. Conversely, if the condenser potential drops below the low limit, the comparator output goes to zero, placing the N-MOSFET in a blocking state and facilitating capacitor charging.

The feedback loop ensures alignment of the PTH pin voltage with the DAC-defined threshold. As a result, the PTH circuit provides the TX microcontroller unit with the capability to dynamically control energy transfer by adjusting the DAC output signal. Refer to Figure 2.15 for a visual representation of the current PTH circuit implementation.

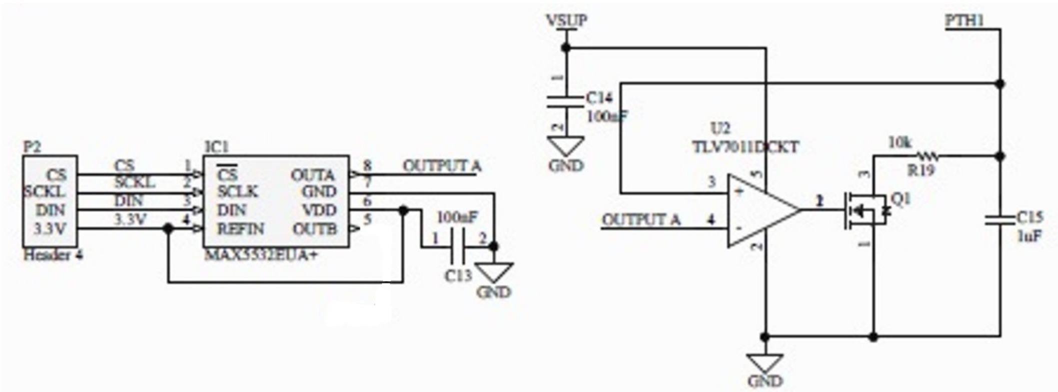

Figure 2.15: PTH Circuit

Then, in [22], the PTHM pin was linked to the secondary output of the DAC, in order to set an upper limit for power transmission. If we apply a voltage to the PTHM pin, when the algorithm update PTH, it will additionally modify PTHM. With this adjustment, we ensure reliability when using different RX coils in the recharge process. Figure 2.16 show the final PTH and PTHM circuit:

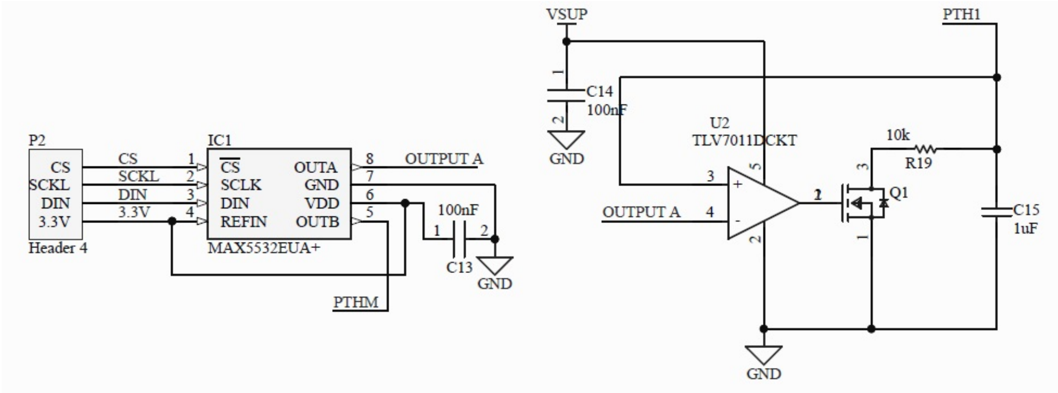

Figure 2.16: PTH and PTHM Circuit

2.5 Self-Powering Supply System

2.5.1 Battery Analysis

In order to ensure the proper operation of our device, it is essential to select the appropriate power supply, which will be chosen meticulously based on our application. Specifically, we intend to test our device in-vivo, and for this reason, using batteries as a power source is convenient from the standpoint of size, comfort, and practicality.

In simple terms, batteries, also known as cells, can be described as a parallel combination of one or more electrochemical cells. Depending on the chemical composition, different electrochemical reactions will occur, and based on this, the battery may or may not be rechargeable. At this point, we can classify them into two groups: primary (non-rechargeable) and secondary (rechargeable) batteries. The main challenge now is to analyse, based on existing literature and previous research, whether primary batteries would be a sustainable option or if it would be more efficient to use secondary ones to meet our energy requirements.

As for primary cells, they are often referred to as 'dry cells' because their electrolyte is not in liquid form but rather in a paste. Due to their non-reversible electrochemical reactions, they are used until their electrode's active components are depleted. Some of their key characteristics include:

- High initial voltage
- High energy density
- Slow discharge rate
- Lightweight

- Low initial cost

Different studies demonstrate why these batteries can be exploited and implemented for biomedical devices. In the article [12], Lithium/iodine batteries prove to be powerful due to their high energy density, making them suitable for implantable cardiac pacemakers. In the case of neurostimulators or drug delivery systems requiring power delivery in the milliwatt range, manganese dioxide batteries exhibit excellent performance with their outstanding storage and discharge characteristics, as well as a high specific energy density.

Furthermore, in another study titled [11], we can observe how defibrillators are powered by lithium silver vanadium oxide batteries, as they meet the main requirements, offering these batteries high pulse power and longevity. However, their irreversible chemical reactions, low C-rate (charge/discharge current rate), and the significant amount of waste generated once they are no longer useful, among other characteristics, prompt us to consider implementing rechargeable batteries for this application.

Secondary batteries, in contrast to primary cells, are constructed with an active material featuring reversible electrochemical properties. This enables the potential for chemical and structural restoration by applying an electrical potential in the opposite direction of the discharge current. The ability to charge and discharge them enhances their lifespan, making them more cost-effective in the long run compared to primary batteries, providing a significant advantage. Specifically for our device, the reduction in size and improved implant longevity makes secondary batteries the optimal choice. Among their other characteristics, we can highlight the following:

- High specific energy
- Good low-temperature performance
- High power density
- Suitable for high-drain applications
- Minimal waste production

However, the primary limitations of these batteries are their complex design, reduced charge retention, lower energy density compared to primary cells, and higher initial costs. Despite these drawbacks, owing to their power output capabilities and, more importantly, their reusability, secondary batteries are rapidly becoming the preferred choice for medical and portable applications. This shift towards improving implant lifetime and size reduction is evident.

In [23], we can observe how Lithium-Ion (Li-Ion) and Polymer Lithium-Ion (Li-Po) batteries are gaining prominence in the biomedical field. Li-Ion batteries were first introduced commercially by Sony Corporation [24] and have since posed a significant challenge to other battery types in portable electronic devices due to their numerous advantages. These advantages include optimal cycling performance, low self-discharge rates, high specific energy, lightweight nature, and a high voltage of 3.6 V. These characteristics make Li-Ion batteries an ideal energy storage solution for small-size portable devices.

Regarding the electrochemical processes in Li-Ion batteries, basically involves the insertion and removal of lithium ions. During discharge, lithium ions migrate from the anode to the cathode, returning to the anode during the charging phase. In a typical Li-Ion battery, the anode is usually composed of carbon-based materials, while the cathode is typically constructed from lithium manganese oxides. Liquid electrolytes in these batteries typically contain lithium salts, leading to our second classification of batteries. When liquid electrolytes are substituted with polymer electrolytes, we obtain Li-Po batteries. Polymer electrolytes improve energy density and efficiency [25], and display remarkable characteristics such as adaptability in size, translucency, low weight, flexibility, and the capability to establish effective connections between electrodes and electrolytes.

In the Table 2.2, an analysis of the Li-Ion and Li-Po batteries is presented with their main characteristics:

Characteristic	**Lithium-Ion (Li-Ion)**	**Polymer Lithium (Li-Po)**
Electrolyte	Liquid electrolyte	Solid-state polymer electrolyte
Specific Energy	High specific energy	High specific energy
Voltage	Typically 3.6 V	Typically 3.7 V
Temperature Performance	Satisfactory	Satisfactory
Power Density	High power density	High power density
Cycle Life	Extended	Extended
Weight	Lightweight	Lightweight
Shape and Size Flexibility	Limited flexibility in shape	High flexibility in shape
Use in Biomedical Devices	Widely utilized	Increasingly favored

Table 2.2: Comparison of Main Characteristics between Lithium-Ion (Li-Ion) and Polymer Lithium (Li-Po) Batteries

Having explained this and considering the specific requirements of our application, the decision is to utilize secondary batteries and conduct research on the two types previously described. Secondary batteries offer several advantages over primary batteries for biomedical portable devices, with the following key reasons:

- Reusability: Secondary batteries can be charged and discharged multiple times, thereby extending their lifespan, reducing overall costs, and minimizing waste, making them a cost-efficient, long-term solution.
- High specific energy: Secondary batteries store a greater amount of energy per unit of volume, which is critical for portable medical devices that require prolonged operation on a single charge.
- Low self-discharge rate: These batteries have a low self-discharge rate, ensuring that stored energy remains available for an extended period, even when the device is not in use.

2.5.2 Charging Profile of Li-Ion and Li-Po batteries

As we have seen previously, both batteries offer an excellent energy-to-volume ratio, providing long life cycles with low self-discharge. Battery charging significantly impacts battery performance and, consequently, their life cycles. Various charging algorithms can be implemented for the charging of these batteries. These algorithms differ in terms of charging time, impact on battery life cycle,charging efficiency, implementation complexity,and cost, as discussed in the paper [26]. The most widely used and the one we will discuss is the constant current-constant voltage (CC/CV) algorithm, which is well-implemented in today's commercial devices due to its ease of implementation.

The CC/CV method consists of applying a constant current to the battery until the battery voltage reaches its maximum charging voltage, which varies depending on the specific battery type. Once this voltage threshold is reached, the charging current will begin to decrease exponentially until it reaches a minimum value; this can be seen in Figure 2.17.

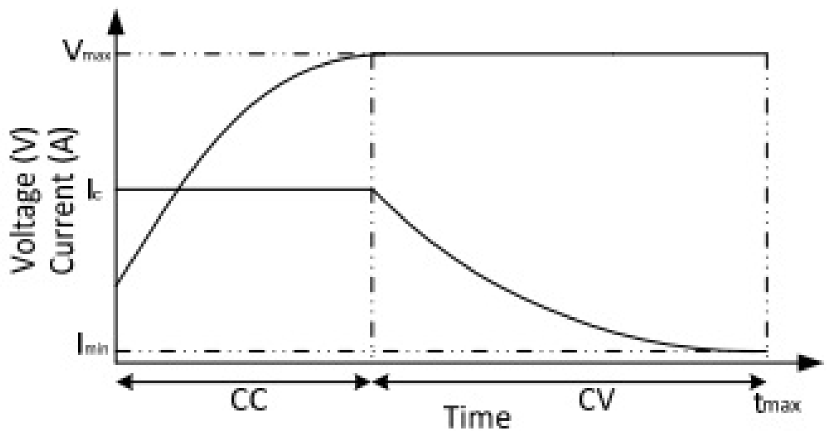

Figure 2.17: Charging Profile of the CC/CV Algorithm

For our applications, we will analyze different CC/CV chargers to supply our system. We will also consider parameters such as the charging current, charger size, and additional features to ensure the correct charging of the battery.

2.5.3 Regulator Analysis

Like all portable medical devices, our device requires a stable reference supply voltage for proper operation, as noted in [27]. To achieve this, we will employ voltage regulators, electronic components designed to control and stabilize the voltage supply, ensuring a consistent and reliable voltage output, even in the face of load variations or input voltage fluctuations. The key considerations for implementing these components in our system are as follows:

- Efficiency: Preventing voltage fluctuations, thus maintaining a stable operational stage for our device.
- Reliability: Enhancing the reliability and lifespan of our system.
- Protection: Shielding our device from potential voltage spikes, surges, and voltage drops.

Existing voltage regulators can be categorized into two primary groups: linear voltage regulators and switching voltage regulators. A comparison of these regulator types is shown in the Table 2.3:

Characteristic	**Linear Regulators**	**Switching Regulators**
Efficiency	Less efficient due to energy dissipation as heat	Highly efficient, less energy dissipation
Output Noise	Low output noise, suitable for low-power applications	May introduce more electrical noise due to switching action
Complexity	Simple and straightforward design	More complex design due to switching circuitry
Input Voltage Range	Suitable for cases where input voltage is close to required output voltage	Suitable for a wider input voltage range

Table 2.3: Comparison of Linear and Switching Voltage Regulators

To power certain biomedical implants, as discussed in [28], linear regulators are often preferred due to their simple design and ability to work effectively with close input and output voltages. However, for our design, we have chosen to incorporate a switching regulator circuit. This choice is based on their capability to achieve high efficiencies, with most of them operating at over 80%, and their ability to regulate output voltages that can be higher, lower, or inverted in comparison to the reference input voltage.This choice aligns with the specific requirements of our application, were high efficiencies are requested to the proper charge of the battery of nDS.

Then, concentrating on the switching voltage regulators, as we have seen before, they are more complex systems but with higher efficiency. We can also divide them into two different groups, depending on if they produce an output voltage lower or higher than the input voltage. They are call buck or step-down regulators and boost or step-up, respectively. Table 2.4 shows a study of their main characteristics:

Characteristic	**Boost Converter**	**Buck Converter**
Voltage Adjustment	Increases output voltage	Reduces output voltage
Efficiency	Typically less efficient due to voltage increase	Typically more efficient due to voltage reduction
Output Current	Lower than input current based on voltage increase	Similar or lower output current based on voltage reduction
Voltage Ripple	May exhibit higher voltage ripple due to voltage boosting	Typically lower voltage ripple due to voltage reduction
Voltage Control	Output voltage is controlled by the duty cycle of the switching element	Output voltage is regulated through feedback control
Inductor Requirement	Requires an inductor to store energy during switching	Utilizes an inductor to smooth current and voltage

Table 2.4: Main Characteristics of Boost and Buck Converters

In Chapter 4, a detailed study of this voltage regulator is conducted, analyzing different models and types, and specifying the various parameters considered for the final selection.

2.6 Final Closed-Loop Wireless Power Transfer System

The entire system we will be working with, previously implemented by [7], [21], and [22], and leveraging the aforementioned NRIC link for WPT and BLE for communication, consists of two integrated circuits. On one side, we have the transmitter, as previously analyzed, which is the LTC4125, while on the other hand, we have the LTC4124 serving as the receiver (RX). The transmitter uses an LC TANK in a series configuration, utilizing the Wurth Electronic coil 760308101104. In contrast, the receiver is characterized by another LC TANK but in a parallel configuration, using the Wurth Electronic coil 760308101220. Additionally, there is nDS, which, along with its battery, is in constant communication with the RX to recharge its battery when necessary. Regarding communication between the RX and TX, both use the MCU CC2640R2F. In an initial version of the TX, the LAUNCHXL-CC2640R2 is used, which is later integrated into another version. In short, as the current closed-loop system is developed in more detail in the following chapters for subsequent modification, it is based on reading data from the RX by the MCU. The MCU then instructs the TX, based on this data, whether to increase or decrease the transmitted power to efficiently perform a recharging cycle. The detailed figure below depicts the entire system, with emphasis on the transmitter, which will be the main focus of this research.

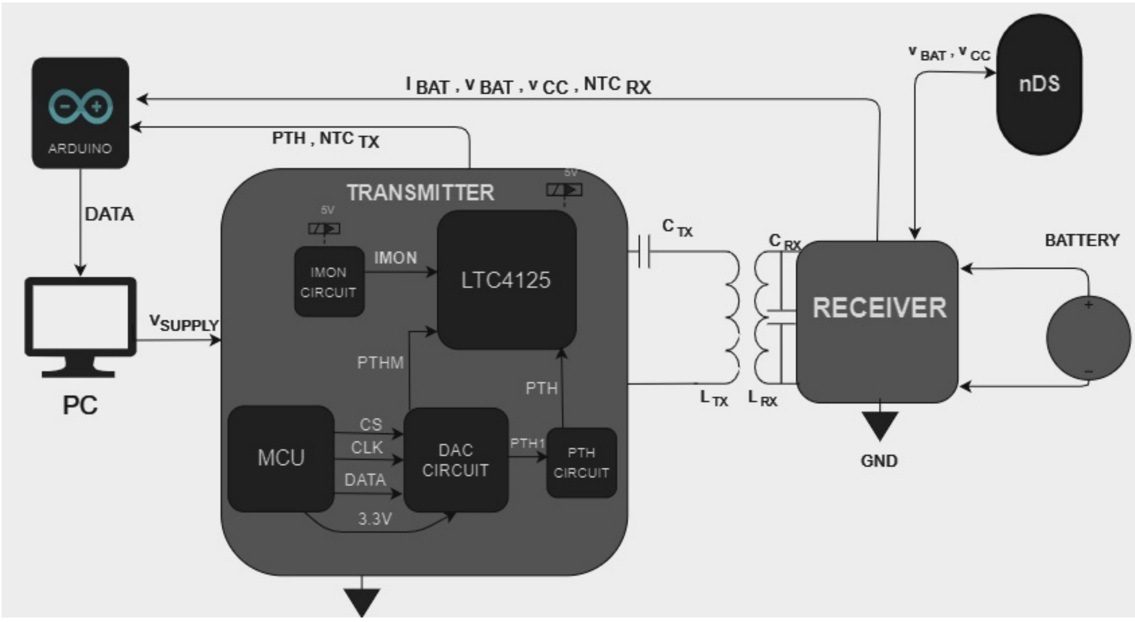

Figure 2.18: Closed-Loop Wireless Power Transfer System

Emphasizing the TX system, in Figure 2.19, we can observe how it will be configured with the various implementations that will be carried out, encompassing functional aspects, power supply, and the constituent blocks:

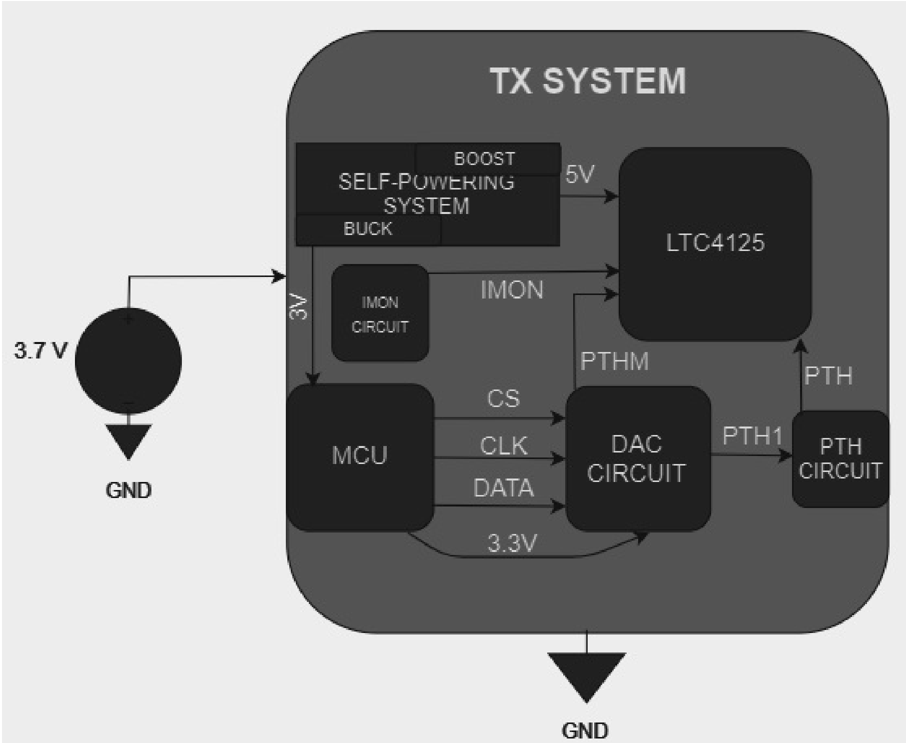

Figure 2.19: The New TX System Blocks

Regarding the hardware, there are three significant changes at the system level for the transmitter. Firstly, the incorporation of the MCU: in the initial version, the LAUNCHXL-CC2640R2 was used, while in the second version, the CC2640R2 is employed for communication. Secondly, at the power supply level, the need for an external power source is eliminated by using a rechargeable battery, and this change includes the implementation of a self-powering system to supply input voltage to the LTC4125 and its associated elements and blocks, as well as the MCU. From a firmware perspective, the primary goal is to transition the device from the central role it played in previous studies such as [7], [21], and [22], and transform it into a peripheral role; this process is detailed and referenced in Chapter 5.

Chapter 3

Transmitter LTC4125 Board Design

In this section, our focus is on the LTC4125 design, where we enumerate all the considerations made during the process to achieve an efficient and robust outcome. It's important to note that two different board versions were designed. Initially, a larger prototype was created to assess critical points and board characteristics, including PTHM voltage, coil temperature, and working frequency. Once all aspects were functioning properly, the final miniaturized version of the LTC4125 board was developed.

Previous works served as references for specific aspects of the system, such as the PTH and PTHM Circuit, and the IMON pin modification implemented by [7], [21], and [22]. In the second version of the board, hardware modifications were also implemented. These included component replacements to address size constraints and the addition of openings to simplify and streamline the assembly process when integrating with other boards.

3.1 PCB Design

3.1.1 PCB Stackup and Considerations

For the design of the boards, we will be using Altium Designer. The first consideration to make is the PCB stack-up that we are going to implement. Since we are working with radio frequency signals (RF), we have decided to use a four-layer PCB, as it offers simple signal routing, as well as complete ground and power planes. The following stack-up is used for both boards:

Layer	Utilization
Top Layer: RF SIGNAL	RF IC and elements, capacitors, RF traces
Layer 2 : GND	Grounding Plane
Layer 3: VCC	Powering Plane
Bottom Layer: NO RF SIGNALS	Other signals and Non-RF elements

Table 3.1: TX LTC4125 Stackup

Allocating a ground plane adjacent to the RF SIGNAL layer minimizes noise and maximizes signal integrity, as it provides low resistance and distributed decoupling capacitance along it. In our case, the LC tank will be our main RF signal, so we must take special care with it to avoid parasitic effects and provide a low impedance return path. In the figure below, we can see the distribution of the layers along the board with a more detailed explanation of each layer:

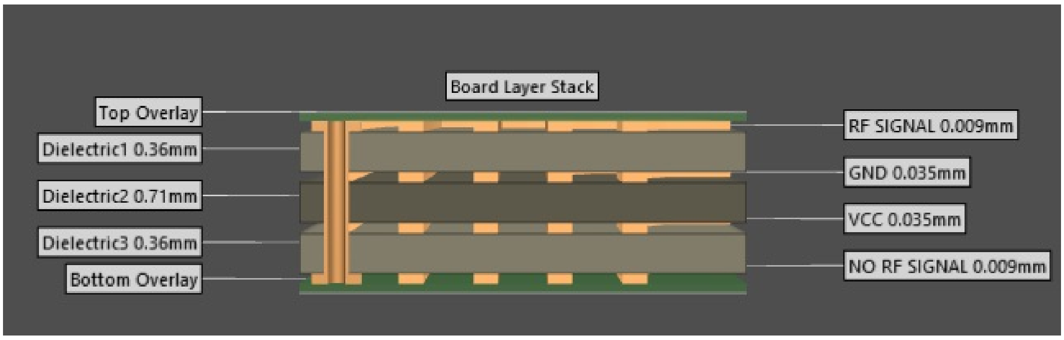

Figure 3.1: TX LTC4125 Layer Stack : Scheme

More technically, in Figure 3.2, we can see the different properties of each layer, including the material, weight, thickness, and dielectric constant of each:

#	Name	Material	Type	Weight	Thickness	Dk
	Top Overlay		Overlay			
	Top Solder	Solder Resist	Solder Mask		0.01016mm	3.5
1	RF SIGNAL	CF-001	Signal	1/4oz	0.009mm	
	Dielectric1	FR-4	Prepreg		0.36mm	4.8
2	GND		Signal	1oz	0.035mm	
	Dielectric2	FR-4	Core		0.71mm	4.8
3	VCC		Signal	1oz	0.035mm	
	Dielectric3	FR-4	Prepreg		0.36mm	4.8
4	NO RF SIGNAL	CF-001	Signal	1/4oz	0.009mm	
	Bottom Solder	Solder Resist	Solder Mask		0.01016mm	3.5
	Bottom Overlay		Overlay			

Figure 3.2: TX LTC4125 Layer Stac-kup: Properties

3.1.2 Signal Integrity Enhancements

To ensure maximum signal integrity, special attention must be given to the design of the LC Tank, with a particular focus on preventing and minimizing crosstalk and interference between the shunt components. To achieve this, the first step, as explained previously, is to place the ground plane adjacent to the LC Tank, providing a low-impedance return path.

Regarding component placement, to minimize parasitic effects, the LC Tank components, namely the capacitors and the inductor, are positioned close to each other. Additionally, to reduce interference, we avoid placing other high-frequency components next to the LC Tank.

In terms of routing, we use short and direct paths for tracing the LC Tank, keeping the traces wide to improve signal transmission and minimize impedance as much as possible.

To achieve an even distribution in the layout, the LTC4125 was positioned in the center of the board. Additionally, the PTH and PTHM circuit was placed at a significant distance from the LC Tank to prevent interference. Various polygon pours were also implemented to enhance electrical performance and heat management, both for the LC Tank and the ground and power planes.

3.2 Performance

3.2.1 LTC4125 Board v1.0

The board prototype is based on version B of the DC2770A-B-KIT from Analog Devices [29]. Additionally, the PTH and PTHM circuit, which has been previously studied in [7], [21], and [22], has been implemented on the board.

For the measurement of coil temperature, a critical factor in preventing overheating, the DC2770A-B-KIT originally used an NTC thermistor, specifically the FTN55XH103FD4B from Murata Manufacturing [20]. Instead, we opted to use a thin-film thermistor, specifically the 103JT-025 from Semitec. This thermistor has a $10k\Omega$ resistance at 25°C and is commonly employed in temperature measurement and control applications [30].

Furthermore, various headers were added to facilitate the monitoring of different parameters in the TX. It's important to note that this is an intermediate step toward achieving the final miniaturized board, as the headers occupy a significant amount of space. These headers include connections for IMON, PTHM, PTH, NTC, FTH, DTH, and FB pins. Additionally, a dedicated header was installed to provide power and SPI control to the DAC (MAX5532EUA) of the PTH and PTHM circuit.

Finally, at Figure 3.3 is shown a complete schematic of the first version of the TX board:

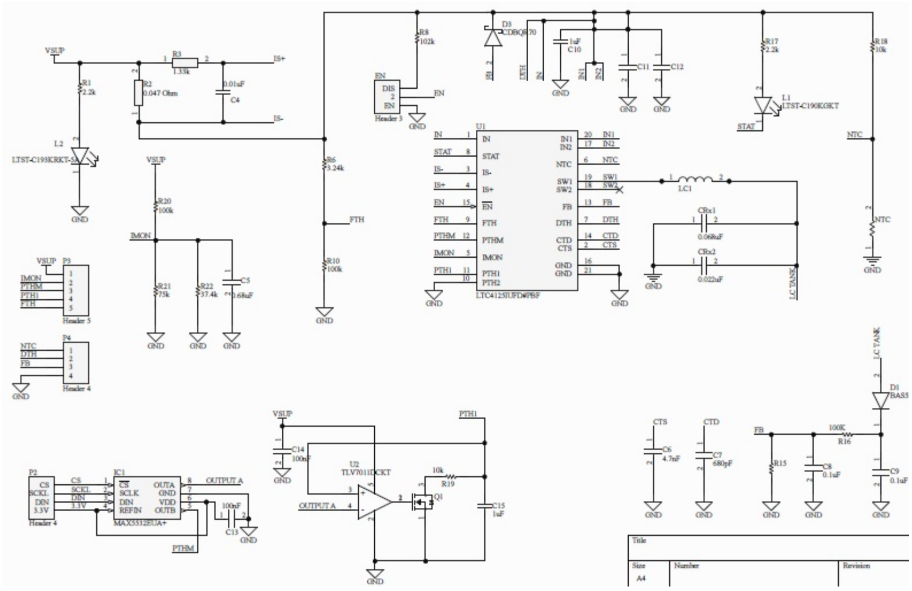

Figure 3.3: TX LTC4125 v1.0 Schematic

Concerning the board, Figure 3.4 displays the final result after taking into account all the considerations mentioned earlier. As you can see, various apertures with a diameter of 3.5 mm each have been strategically placed. This was done to facilitate the attachment of the TX to the corresponding RX, ensuring a precise alignment with the coil. Notably, the TX coil was intentionally positioned in this location for this specific application. As for the NTC thermistor, it was positioned in a manner that allows the sensor to be attached perfectly to the center of the coil. This placement ensures precise temperature measurement. The board final dimensions are 125 mm x 75 mm x 1.6 mm.

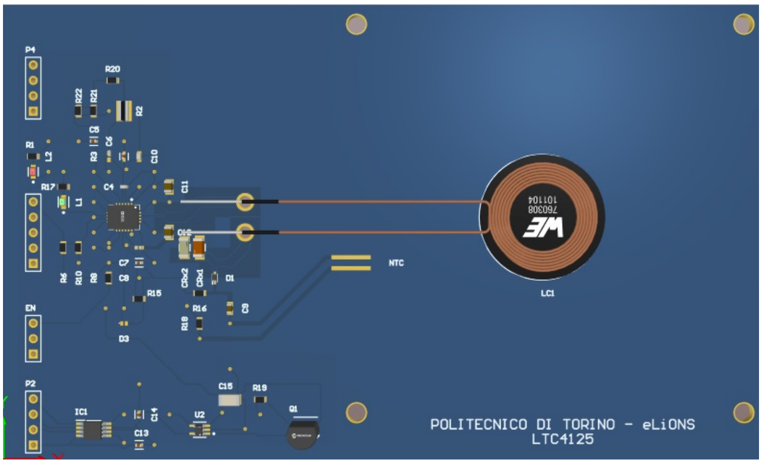

Figure 3.4: TX LTC4125 v1.0 Board

3.2.2 LTC4125 Board v2.0

Considering the goal of minimizing the board's size in comparison to the previous version depicted in Figure 3.4 several modifications are necessary to streamline the design. Broadly speaking, all the headers will be removed and replaced with pads, some components will be relocated to the bottom of the board, and certain elements will be substituted due to size constraints.Considering the final packaging, certain design elements have been thoughtfully incorporated to ensure the robustness of the entire system's packaging.

3.2.2.1 Hardware Modifications

The first modified element is the N-MOSFET (TN0702) from the PTH and PTHM circuit, which is used to discharge the PTH pin capacitor. This change was not made for functional reasons but rather due to size constraints. The TN0702 package (TO-92) has a height of 20mm, so the primary objective is to find an equivalent component with similar characteristics to minimize the space it occupies. To achieve this, alternative packaging options are being considered. The main characteristics we are looking for in selecting the new MOSFET are [31]:

- Polarity: N-channel
- Number of channels: 1 channel
- Vds >= 5 V (because our supply voltage is 5V, even though the MOSFET we are currently using has Vds=20V)
- Id approximately or bigger than 530 mA

- Vgs(threshold) = 1V
- Rds approximately 1.3 ohms
- SMD Mounting

Taking these factors into account and considering the commercially available components, we have decided to replace the TN0702 with the NTR4501NT1G from ON Semiconductor [32]. The properties of this MOSFET are presented in Table 3.2:

Parameter	**Value**
FET Type	N-Channel
Technology	MOSFET (Metal Oxide)
Drain to Source Voltage (Vdss)	20 V
Current - Continuous Drain (Id) @ 25°C	3.2A (Ta)
Drive Voltage (Max Rds On, Min Rds On)	1.8V, 4.5V
Rds On (Max) @ Id, Vgs	80mOhm @ 3.6A, 4.5V
Vgs(th) (Max) @ Id	1.2V @ 250µA
Gate Charge (Qg) (Max) @ Vgs	6 nC @ 4.5 V
Vgs (Max)	±12V
Input Capacitance (Ciss) (Max) @ Vds	200 pF @ 10 V
Power Dissipation (Max)	1.25W (Tj)
Operating Temperature	-55°C 150°C (TJ)
Mounting Type	Surface Mount
Package	SOT-23-3 (TO-236)

Table 3.2: NTR4501NT1G Specifications

This MOSFET meets the required parameters, comes in an SOT-23-3 package, and has a height of 1.1mm, ensuring compliance with size constraints.

Continuing the analysis of the PTH and PTHM circuit block, a significant change compared to the first version of the board is the removal of the DAC (MAX5532EUA). In this new version of the TX board, we will not incorporate this component as we plan to leverage its functionality on the nDS board. Taking into consideration the perspective of the final system, we will take advantage of the fact that on the nDS board, we already have the MCU (CC2640R2F), and the DAC (MAX5532), along with a 2.4 Gigahertz antenna [7], [4]. Since this part of the system is already designed, implemented, and tested, and with the aim of simplifying our design and proceeding with miniaturization, we have decided to remove the DAC from the initial board and directly utilize the components from the nDS that are essential to complete our system. In this case, it includes the MCU, DAC, and the 2.4GHz antenna.Figures 3.5 and 3.6 show the PTH and PTHM circuit before and after the change:

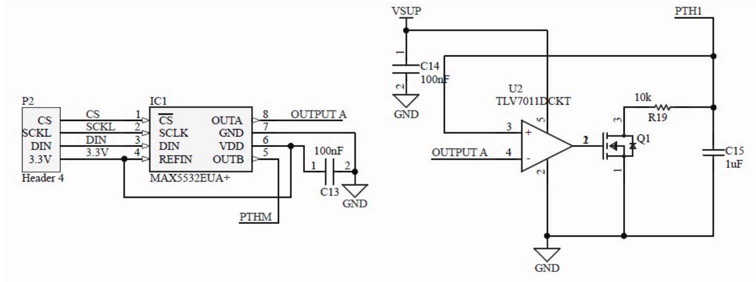

Figure 3.5: PTH and PTHM Circuit Before

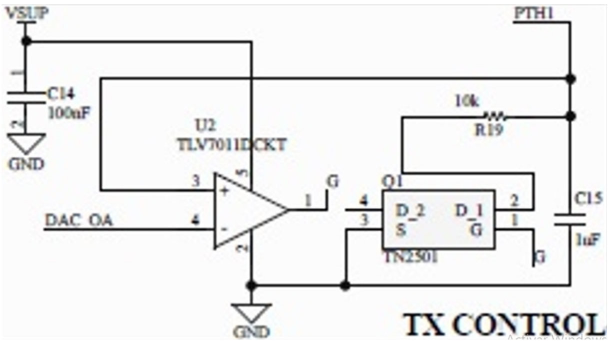

Figure 3.6: PTH and PTHM Circuit After

To further reduce the size of the board, two crucial components are planned to be positioned on the bottom side of the board. One of these elements is the NTC thermistor 103JT-025 from Semitec, while the other is the coil 760308101104 from Wurth Elektronik [33]. The coil is placed in the center of the bottom side to achieve a balanced layout, while the NTC thermistor is positioned beneath the coil to ensure precise temperature measurement. On the back of the board, a cross and a semicircle are marked to determine the exact location for the coil placement. Lastly, as mentioned earlier, headers are replaced with pads to further minimize the dimensions of the final board. Another pad was also added to connect the outputs of the nDS DAC to the inputs of the TX control block circuit. Additionally, a solder bridge was implemented for potential TX enable activation. These pads are strategically positioned to use the fewest possible wires.

3.2.2.2 LTC4125 Final Board v2.0

In Figure 3.7, we can see the complete schematic of the final version of the TX board, incorporating all the previously mentioned considerations. As we can observe, and to simplify the schematic analysis, the system is divided into various functional blocks:

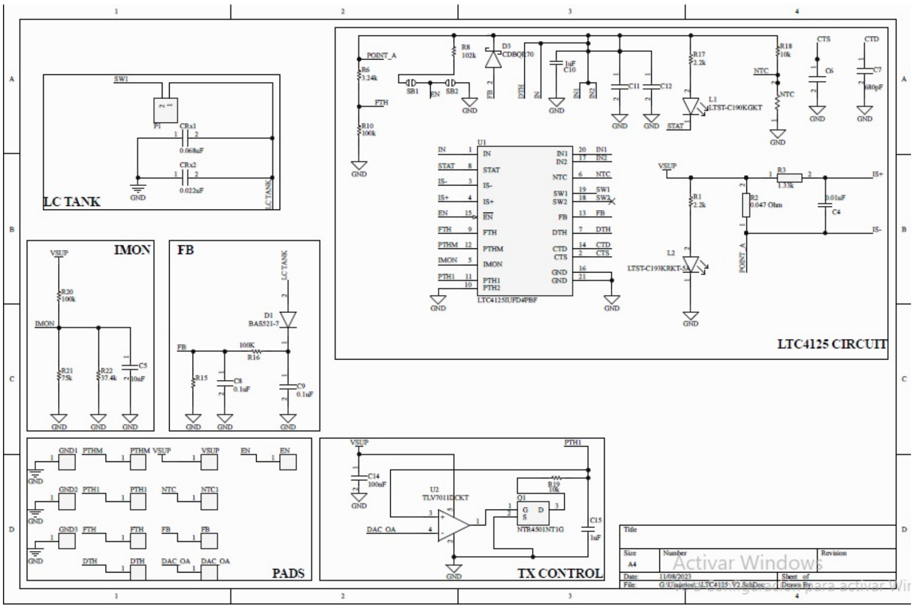

Figure 3.7: TX LTC4125 v2.0 Schematic

In the two figures below, we can observe the final design of the LTC4125 TX board with all the previously mentioned changes. As we can see, once again considering the packaging of the entire system, various holes have been strategically placed for the assembly of the different boards that comprise the final system, namely the battery charger and the SPS. These openings have a diameter of 2.5 mm and do not affect the functionality of our circuit in any way.The final dimensions of the board are 33.8 mm x 34.5 mm.

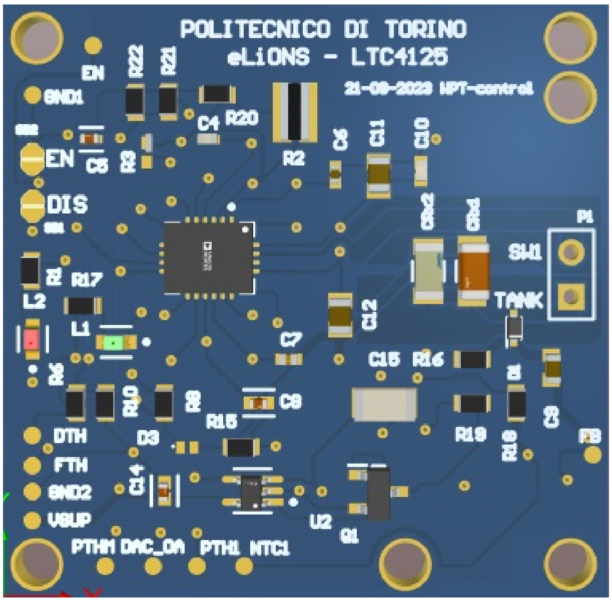

Figure 3.8: TX LTC4125 v2.0 Board: TOP

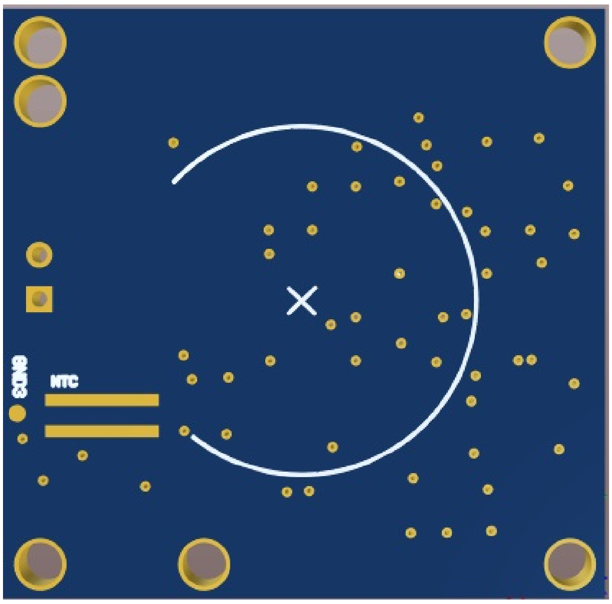

Figure 3.9: TX LTC4125 v2.0 Board: BOTTOM

Chapter 4

Self-Powering System

To effectively design our SPS, our first step is to characterize the system's needs and specifications, ensuring a robust and efficient design. From a portability perspective, the incorporation of a battery is essential, given that the device's ultimate purpose is for in-vivo tests, making a portable power source a primary requirement. In terms of power supply, it's crucial to consider that we are working with components that have varying input voltage requirements. Therefore, it may be advantageous to explore the use of voltage regulators to produce stable voltage outputs that match to the needs of each component.

In this chapter, we will make a rigours selection process to choose the most suitable battery for our system,ensuring it meets all requirements in terms of current and power levels. Additionally,different voltage regulators are going to be studied, ultimately selecting the most appropriate ones for each component. This meticulous approach will guarantee the proper operation of each component. Finally, taking into account not only the components selected but also the final system requirements, the design of the board is completed. We will also explain the various considerations made to achieve the final device.

4.1 Battery Selection

4.1.1 System Analysis and Considerations

In order to proceed with the battery selection, two important pieces of data must be taken into account to calculate the minimum capacity required for our battery to power our system. First, we need to consider the current required by our device, and then we must determine the amount of time our device needs to deliver power to the RX. It is essential to always keep in mind whether the battery of the nDS is charging to utilize its maximum load capacity.

We know that battery capacity can be defined as:

$$C_{BAT} = I[A] * time[hours] \tag{4.1}$$

When it comes to current, we should not only consider the current consumption of the TX but also the input current it will require. As mentioned before, we are not directly powering the transmitter from the battery. Instead, we will use voltage regulators to ensure a stable voltage input for each component. In this context, the efficiency of the voltage regulator is a critical factor in battery selection. Depending on its efficiency, the required battery capacity may vary because the output of the voltage regulator determines the actual input current for the TX.

A block diagram of the system can be represented as shown in Figure 4.1:

Figure 4.1: Supply Block Scheme

For this analysis, we will consider two fundamental design parameters as input. The first is the battery's output voltage, which is set at 3.7V. As we discussed earlier, most Li-Ion and Lithium Polymer batteries have an output voltage around this value, making it our reference for the analysis. Secondly, for the efficiency of the voltage regulator, we will take a precautionary estimate of 80%.

Taking into consideration this parameters, we can redefine the Fig.4.1 as:

Figure 4.2: Detailed Supply Block Scheme

Also, redefining Eq. 4.1 for our specific case:

$$C_{BAT} = I_{INBoost}[A] * time[hours] \tag{4.2}$$

Where we can determinate $I_{INBoost}$ as:

$$
\begin{aligned}
I_{INBoost} &= \frac{P_{OUT}[W]}{V_{INBoost}[V] * \eta}[A] \\
&= \frac{I_{TX}[A] * V_{TX}[V]}{V_{INBoost}[V] * \eta}[A]
\end{aligned}
\tag{4.3}
$$

According to [7], the maximum power transmission of the TX during a charge test of the nDS battery at $10mA$ is $210mW$ for a separation of $6.5mm$ between the TX and RX. We are using this parameter as a reference. Furthermore, we will incorporate a safety margin by increasing the maximum TX power by 50% to ensure smooth battery charging without any issues. With this consideration we will work with a $315mW$ transmission power to model the capacity of the battery. Then, Eq.:

$$
\begin{aligned}
I_{INBoost} &= \frac{315[mW]}{3.7[V] * 0.8}[A] \\
I_{INBoost} &= 106[mA]
\end{aligned}
\tag{4.4}
$$

In addition, we must also take into account the current consumption of other components, such as the TX microcontroller. According to [7], it has an average consumption of 5mA. Based on this information,and as a safety measure, the Boost input current will be consider as:

$$
I_{INBoost} = 200[mA] \tag{4.5}
$$

In addition to current, another aspect under investigation is the charging time. According to both [7] and [22], we reach a full battery charging cycle after 250 minutes (4 hours) for a specific 25mAh battery ($LIR2025$) using a 10mA charging current. Finally,considering Eq. the minimum battery capacity should be:

$$
\begin{aligned}
C_{BAT} &= 200[mA] * 4[hours] \\
&= 800[mAH]
\end{aligned}
\tag{4.6}
$$

If we consider the worst case, according to [22], the TX battery must last at least one recharge cycle of the RX battery,which consists of a constant current phase (CC) and constant voltage phase (CV). From the data we have from [7] and [22], a single charge cycle of the RX battery lasts 4 hours in the CC phase. After 4 hours, the LTC4124 initiates a three hours timer, after which it automatically switches the battery to the CV discharge phase. So, from the LTC4124's perspective, a recharge cycle includes also the 3 hours provided by the LTC4124's internal timer [34].So, from a worst case perspective view, the capacity of our battery should be at least of:

$$\begin{aligned} C_{BAT} &= 200[mA] * (4+3)[hours] \\ &= 1400[mAH] \end{aligned} \tag{4.7}$$

With this value in consideration, we are able to perform an analysis for the battery selection, in order to use the most suitable one for our application.

4.1.2 Battery Selection

Starting with the assumption that we possess a predetermined capacity value for our target battery, the subsequent step involves an analysis of the batteries available in the market. This assessment will not be limited just to this parameter but will also include other factors, including the battery's chemical composition, charging and discharging currents, and, most importantly, its physical dimensions.

In the context of our system, it is essential to reiterate once more that its intended use is for in-vivo testing . Consequently, the dimensions of the battery assume an important role, as our objective is to maximize capacity while minimizing overall volume.Our primary research was focused on rechargeable batteries, specifically Lithium-ion (Li-ion) batteries and Lithium Polymer (Li-Po) batteries, as these are the most suitable options for AIMDs applications. It is important to emphasize that our efforts were concentrated on the search for commercially available batteries currently present in the market. In order to choose the battery, the following parameters were taken into account:

- Battery Capacity
- Battery Chemistry
- Maximum Charge Current
- Maximum Discharge Current
- Size
- Weight

The primary battery procurement sources in our research are RS Components and Transfer Multisort Elektronik (TME). Form this distributors, on Tables 4.1 we list the batteries taking into consideration:

Battery	Nominal Voltage [V]	Capacity [mAh]	Chemistry	Size	Weight	Max. Charge I	Max. Discharge I
FT103450P	3.7	1800	LI-PO	67mm x 10.4 mm x 35 mm	36g	0.85 A	0.85 A
SR674361P	3.7	2000	LI-PO	7mm x 43.5 mm x 63 mm	40g	1 A	2 A
ICR18650-260PCM	3.7	2600	LI-ION	Height: 69.0 mm ϕ : 18.5mm	50g	5 A	15 A
ICR18650-26JM	3.63	2600	LI-ION	Height: 65.0 mm ϕ : 18.40mm	50g	2.6 A	5.2 A

Table 4.1: Battery Specifications

From this batteries, and considering our design parameters, the SR674361P Li-PO Battery was chosen, since this battery encompasses all the necessary features for the operation of our system [35]. It has the following characteristics:

Parameter	Value
Nominal Voltage	3.7 V
Capacity	1800 mAh
Chemistry	LI-PO
Size	67mm x 10.4mm x 35mm
Weight	36g
Max. Charge Current	0.85 A
Max. Discharge Current	0.85 A

Table 4.2: SR674361P Specifications

Also, according to [35], the physical dimensions of the SR674361P battery are:

Item	Dimension (mm)
T	Max 7.0
W	Max 43.3
L1	Max 62.0
L2	8±1
M	14±1.5
N	4.0±0.2

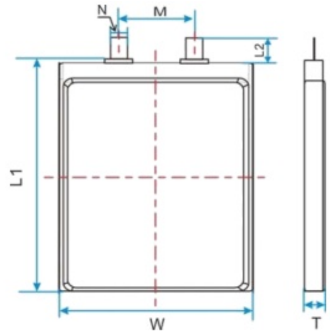

Figure 4.3: SR674361P Dimensions [35]

The parameters depicted in the Fig.4.3 will play a crucial role in shaping the transmitter's packaging during the final stage of design.

4.1.3 Battery Charger Selection

In our effort to select the most suitable battery charger, our primary goal is to find a commercial board that ensures the correct charging of our battery. Two critical constraints guide our selection process. The first constraint is related to battery chemistry. Charging a Li-Po battery with a charger that is not compatible with Li-Po chemistry can lead to various issues, including overcharging, incorrect voltages, and a reduced battery lifespan. The second constraint pertains to the size of the board, as dimensions play a vital role in packaging the final system.

For our analysis, we considered two board models: the DRF0208 Charger [36] by DFOBOT and the Adafruit 4410 Charger [37]. Both models possess features that align with the requirements of our specific application. The comparison Table 4.3 highlights the key characteristics:

Characteristic	**Charger DRF0208**	**Adafruit 4410 Charger**
Programmable Charge Current	Up to 1000mA	100mA (adjustable to 500mA)
Constant-Current/Constant-Voltage	Yes	Yes
Types of Battery	Single-cell Li-Ion or Li-Polymer batteries	Lithium Ion/Lithium Polymer 3.7/4.2V batteries
Input Interface	Micro USB	USB Type C
Battery Connector	JST-type or terminal	JST plug
Size	3.2x2.7x1cm (1.26"x1.06"x0.39")	2.4x 1.9 x0.72cm (0.9" x 0.7"x 0.3")
Voltage Accuracy	1.5% @ Preset 4.2V Charge Voltage	Not specified
Operating Temperature Range	-40°C to 85°C	Not specified
USB Type	Micro USB	USB Type C

Table 4.3: DFR0208 and Adafruit 4410 Characteristics

The Table.4.3 reveals that both chargers are compatible with both Li-Po and Li-Ion batteries. Concerning size, both options meet our requirements, with the Adafruit 4410 Charger being notably more compact than the DRF0208 Charger. Examining the electrical specifications, the DRF0208 Charger supports a programmable charge current of up to 1A, while the Adafruit 4410 Charger can be adjusted up to 0.5A. Based on this information, we have chosen to work with the DRF0208 Charger, as it enables our battery to charge in half the time compared to what we can expect from a full charge using the Adafruit 4410 Charger. Figure 4.4 revels the final aspect and sizes of the chosen charger:

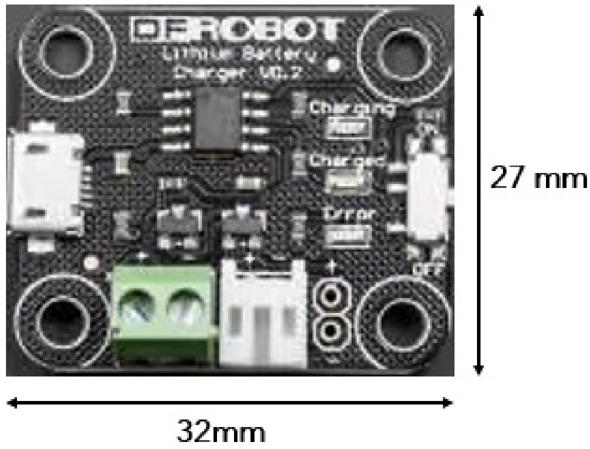

Figure 4.4: DRF0208: Facet and sizes [36]

4.2 Voltage Regulators Selection

In order to proceed with the design of the final SPS board, it is crucial to begin by selecting its main components. In this case, voltage regulators take on special significance. As we mentioned at the beginning of this chapter, our final transmitter system is composed of components that require different levels of supply voltage. Therefore, we need to use voltage regulators to convert the battery's output voltage to the required voltage levels. In this section, we will address the analysis of various voltage regulators, outlining the requirements of each specific block and selecting the final components for the SPS.

4.2.1 Boost Regulator Evaluation

The primary component in our system is undoubtedly the LTC4125. According to the [18], it has an input voltage range of $3V$ to $5.5V$. However, as in previous works such as [7], [21] and [22], we will operate with an input voltage of $5V$. In terms of input current, according to the [18], it has a maximum input current of 0.5A. Nonetheless, from Equation 4.5, we can determine that our system will operate with a maximum current of $0.2A$.With these two specifications as our input parameters, and considering our previously selected $3.7V$ Li-Po battery, we can conclude that a Boost regulator is required to raise the battery's output voltage from $3.7V$ to $5V$. Additionally, when choosing the battery for our system, we assumed various specifications for minimum efficiency in the capacity calculation. Therefore, this is another crucial factor to take into account. Once again, we perform an analysis of commercial components to identify the most suitable Boost regulator for our application. Table 4.4 highlights the main characteristics of some regulators that fit with our application:

Characteristic	**MCP16251/2**	**TPS61023**	**LTC3105**
Input Voltage Range	0.35V to 5.5V	1.8V to 5.5V	1.8V to 5.5V
Output Voltage Range	1.2V to 5.5V	1.2V to 5.5V	1.8V to 5V
Output Current	Up to 500mA	Up to 1.5A	Up to 200mA
Efficiency	Up to 90%	Up to 95%	Up to 90%
Quiescent Current	19µA	50µA	680nA
Shutdown Function	Yes	Yes	Yes
Package	SOT-23, DFN-10, MSOP	SOT-23, QFN-10	SOT-23, DFN-6, MSOP
Advantages	High efficiency, wide input range, low quiescent current	Wide input range, compact, versatile	Low quiescent current, multiple packages
Disadvantages	Lower output current	Limited output current, lower efficiency	Limited output current, limited output voltage range

Table 4.4: Boost Regulators Specifications

We can observe in Table 4.4 that all three of them meet the previously mentioned requirements. However, we have chosen to work with the TPS61023 [38], as it exhibits the highest efficiency (up to 96%) and the greatest output current capacity (up to 1.5A). Specifically, in our case, we need to consider the actual efficiency for the input voltage we are working with. You can see the efficiency of the TPS61023 in the Figure 4.5 [38]:

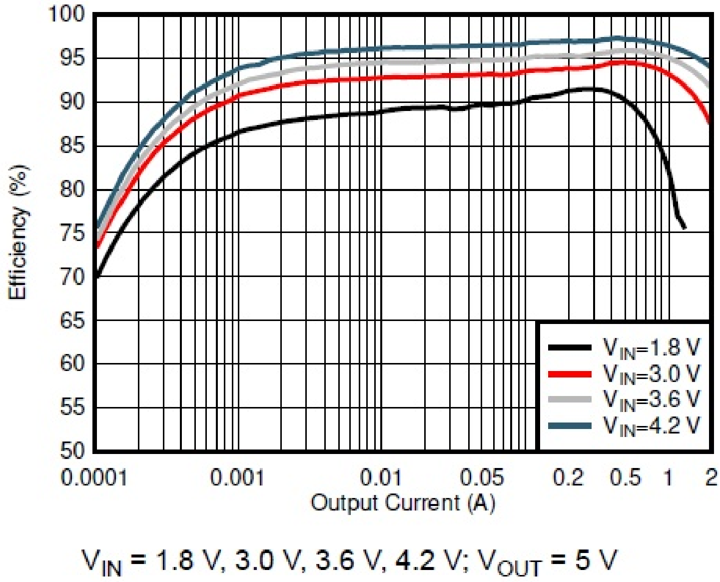

Figure 4.5: TPS61023 Load Efficiency With Different Inputs [38]

As shown, the efficiency for an input voltage of 3.7V is above 90%. Therefore, the Boost regulator meets the efficiency requirement for the current range our system operates within. The TPS61023 can provide an output of $5V$ and $1.5A$ from a Li-Po battery, following the typical application in Figure 4.6, given by [38]:

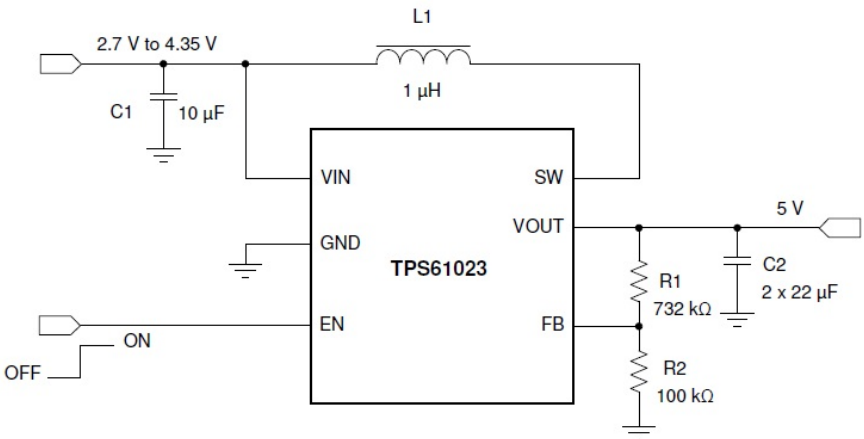

Figure 4.6: TPS61023 5V Boost Converter: Typical Application

The schematic shown in Figure 4.6 is the one we will implement in the final SPS board, in order to supply the LTC4125.

4.2.2 Buck Regulator Evaluation

Another element into consideration is the TX microcontroller. In this case, as studied before in [7] and [22], and according to [29], we will require a power supply of 3V and an input current of $10mA$. We will exploit the use of the TPS82740B from Texas Instruments as it was used before in a previous work [22]. The TPS82740B has the following characteristics [39]:

Characteristic	**TPS82740B**
Input Voltage	2.7V to 5.5V
Output Voltage	Adjustable (0.9V to 3.3V)
Output Current	Up to 400mA
Efficiency	Up to 95%
Package	MicroSIP
Size	2.3mm x 2.9mm

Table 4.5: TPS82740B Specifications

As in previous works, capacitors were placed in the input and in the output to ensure signal stability. A schematic can be shown below:

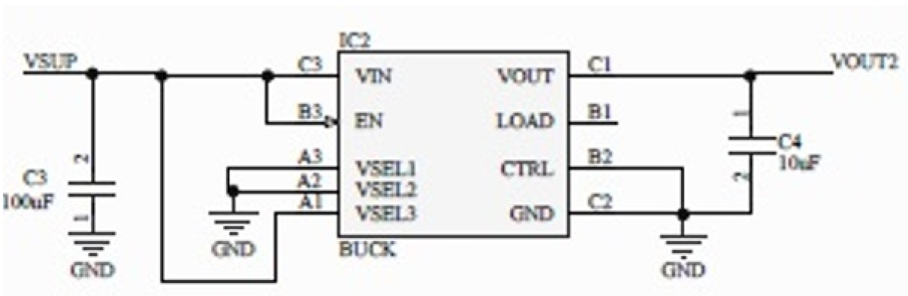

Figure 4.7: TPS82740B Scheme

4.3 SPS Board Design

The design of the SPS Board primarily focuses on implementing the Boost and Buck voltage regulators that were previously selected in Section 4.2. This is done to provide a stable input voltage for the LTC4125 and the TX microcontroller. In the board design, various considerations were taken into account, spanning from component placement to board size and layer configuration. A block diagram is provided below to illustrate the main components:

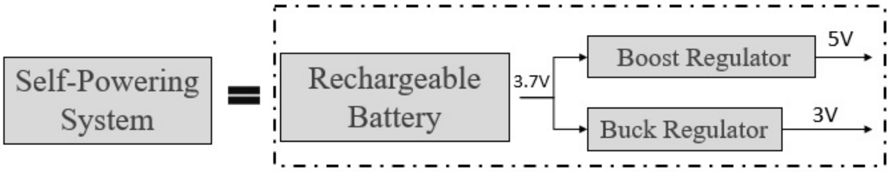

Figure 4.8: SPS Block Scheme

4.3.1 PCB Design and Considerations

Once again, for the PCB design we use Altium Designer. To start with, first we need to establish the schematic of the hole system, which we can see in the next figure:

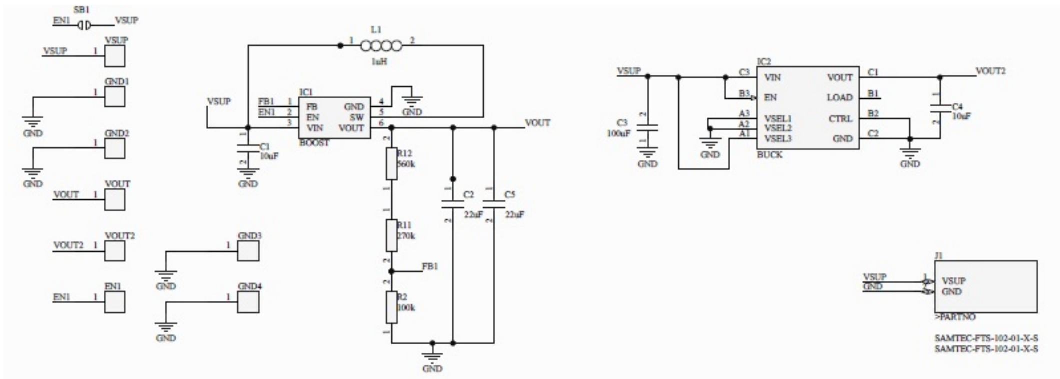

Figure 4.9: Self-Powering System Schematic

We can observe two main blocks in the design. One consists of the Boost circuit, as depicted in Figure 4.6. The other comprises the Buck circuit, illustrated in the previously explained Figure 4.7. Additionally, various pads are visible, including one for the battery supply, three for grounding, and separate pads for the output of the Boost and Buck converters. Furthermore, there is a dedicated PAD for enabling the Boost converter, which can be activated either via a solder bridge or through software.

With the schematic of the circuit completed, we can now proceed to PCB design. However, before diving into the design process, we need to consider a few important factors. One of the key considerations is the PCB's dimensions. To ensure an efficient use of space within the final system package, we must determine the optimal size for our board while taking into account all the other boards that will be housed within the same package, including the LTC4125 board, battery charger, and nDS. To maximize space utilization, the following layout is proposed:

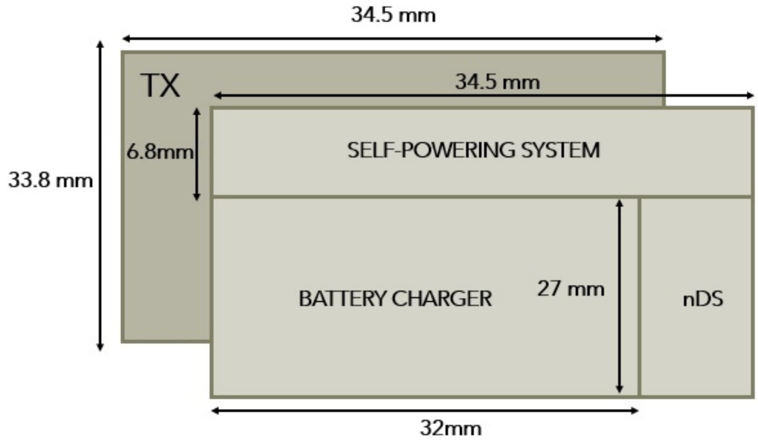

Figure 4.10: Final Layout

We now have the dimensions of our SPS board: 34.5 mm x 6.8 mm. Considering these dimensions and the size of the components we're working with, we need to plan for their placement on both the upper and lower layers of the PCB. From a technical perspective, a two-layer PCB is employed. In contrast to the LTC4125 board, the SPS board can effectively utilize a two-layer stack. The top layer is designated for signals and power distribution, while the bottom layer is dedicated to grounding, with a ground pour designed to reduce impedance between the signal lines. The placement of pads has been strategically arranged to facilitate the shortest possible wire connections to other boards. Some pads are located on the top layer, while others are positioned on the bottom. The thickness of this two-layer stack is approximately 0.5mm.

4.3.2 Performance

After considering all the factors mentioned earlier and paying attention to the arrangement of all the elements to create a more compact and robust design, Figure 4.11 and Figure 4.12 depict the top and bottom views of the final Self-Powering System, respectively. As observed, this board also incorporates strategically placed holes. These openings serve to simplify and streamline the assembly process when integrating with other boards. Much like the transmitter and the battery charger, the SPS features its own corresponding apertures. These openings are designed for use during assembly, enabling the incorporation of additional elements to securely interconnect all components in a more robust manner. Finally, a connector (FTS-102-01-L-S) has been installed on the board to allow for the possible connection and disconnection of the battery from the rest of the system, if necessary.

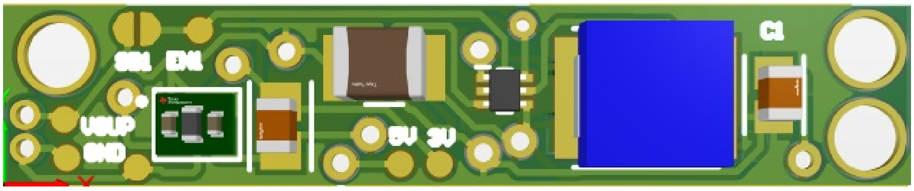

Figure 4.11: SPS Board: Top View

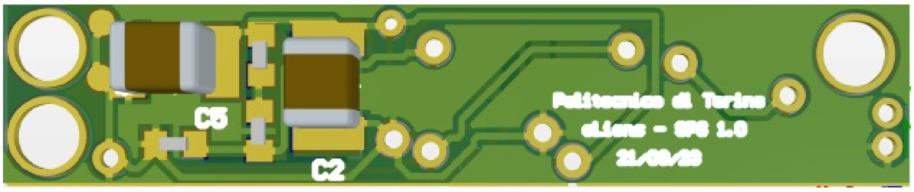

Figure 4.12: SPS Board: Bottom View

Chapter 5

Migration of the TX to a Peripheral Role

5.1 Motivations of the transformation

Currently, several battery charging cycles for the nDS have been conducted, where our TX plays a central role, while the RX assumes a peripheral role, achieving a perfect closed-loop control [7],[22]. Essentially, the MCU of the RX periodically sends notifications to the TX, informing it when to decrease or increase the transmitted power value based on the monitoring of two specific parameters: V_{CC} and V_{BAT}, where the former is the rectified output voltage of the LTC4124, while the latter corresponds to the battery voltage [7].

Moreover, to analyze whether the battery charging was successful or if there were issues during the recharge, it is necessary to acquire various parameters from both the TX and the RX. Regarding the receiver's side, data such as battery voltage and current, as well as the value of V_{CC}, are crucial for this analysis. On the other hand, from the TX side, temperature data and the value of the PTH pin are necessary for a comprehensive analysis. Currently, these data are collected using a third microcontroller, which is connected to both the TX and RX to obtain the aforementioned parameters, as illustrates Figure 5.1. While the system functions for data collection, it is not practical for our application, as manipulating the devices directly with cables each time we want to collect data is inconvenient. Additionally, it becomes impossible to measure them in an in-vivo test where the individual undergoing the test may be moving, resulting in discomfort and potentially unreliable results.

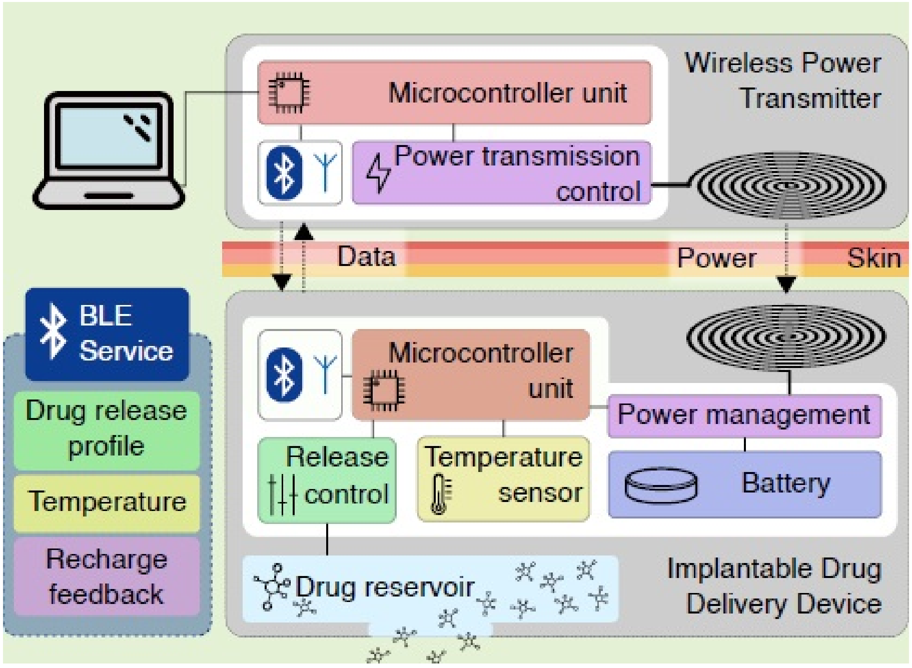

Figure 5.1: Complete Actual System [40]

With the aim of having complete control over our system without direct manipulation and the ability to collect real-time data during an in-vivo test, the motivation arises to migrate our TX from the central role it currently performs to a peripheral role. In general terms, and with a more detailed analysis to follow, we will configure our TX in such a way that it only has control over increasing or decreasing the transmitted power to our RX, without directly communicating with it. In this case, another MCU will handle the communication between these two devices, taking on the central role. It will receive notifications from the RX (which was previously done by the TX) and, based on these notifications, give an order to the transmitter to raise, lower or retain the transmission value.

These changes in the peripheral role not only enhance the IoT capabilities of our system but also simplify and facilitate remote monitoring and control, as well as enhance the user experience, ensuring non-invasive and patient-friendly healthcare. Finally, and as a fundamental pillar of this change, we achieve the ability to perform in-vivo tests with our complete closed-loop WPT system. In the image below, a basic block diagram is presented to illustrate how the new system would be structured. This will be detailed in the upcoming sections, culminating in a final display of the system, where each block will be outlined, specifying its functions and role.

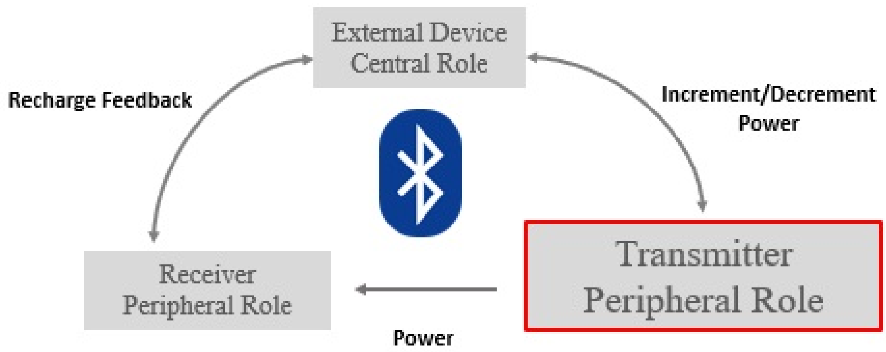

Figure 5.2: Basic Block Diagram

5.2 First Steps for the shift

As mentioned earlier, currently, the TX and the RX require the physical connection of a third device for the real-time collection of their various parameters, making it impossible to perform in-vivo tests of our WPT.

To facilitate the analysis and subsequent migration of the role of our transmission, it is necessary to divide the essential activities performed by each device to charge the nDS battery. This division helps to have a clear understanding of which characteristics should remain in the TX and which should not. With our objective being the manipulation of the TX, we will focus on the characteristics of the RX that enable its communication and control.

Essentially, the RX is responsible for notifying, through a variable called THR, whether the TX should increase or decrease the transmitted power value. From this perspective, nothing changes for the migration of the TX since, instead of notifying the TX, we now need to notify the new central device, and it will transmit the necessary information to the TX. Regarding the TX, in its new central role, once connected to the RX, it waits for notifications from the RX to make a decision regarding power control. This is where we will focus on the migration of the device's role. In a new implementation as a peripheral, we will implement the same code for increasing and decreasing power, but instead of being received as before, we will leverage the services and characteristics of BLE to receive this value that currently comes from the RX but from the new central device. Additionally, other parameters can also be written or read from these characteristics to have a more robust control of our TX. The following section details the characteristics and parameters used, as well as how they were implemented.

5.3 TX as a Peripheral Role

Fundamentally, for the control of transmitted power, the PTH and PTHM circuits are used, as explained in Chapter 3, previously implemented by [7] and [22]. This circuit essentially exploits the two outputs of an analog-to-digital converter to set the values of the PTH and PTHM pins. Through these two pins, we achieve the increase or decrease of power, making the control of the DAC a parameter that must be considered as a first step for the migration. Secondly, one of the fault conditions of the LTC4125 is the working temperature, which must be below approximately 42°C [18]. Currently, the value of this parameter is obtained using a cable connected from the TX to the MCU responsible for collecting real-time data. By setting the TX as a peripheral, the use of this cable will no longer be possible, so another method must be employed to obtain this value.

With the chosen essential parameters, we can proceed to manage them, for which we will make use of the system's characteristics. Taking the control of the digital to analog converter (DAC) as the first parameter, we know that to modify its output values, it expects a control variable to determine what to do. Therefore, a writable characteristic should be implemented for DAC management. This way, the TX would receive a value through a characteristic from the central device, instructing it on what to do with the two DAC outputs. In particular, there are three commands that the TX will receive through a characteristic:

- MAINTAIN THRESHOLD: 0x00
- DECREASE THRESHOLD: 0x01
- INCREASE THRESHOLD: 0x02

Depending on this value, the transmitted power will change as a consequence of updating the DAC output voltage values. On the other hand, not for functional but application reasons, and to continue exploiting the features, we will display, in another characteristic, this time in read mode and as a notification, the value received by the central device on the TX. This provides a way to observe whether the DAC behavior is consistent with the command received from the central device. Furthermore, the output voltage of the DAC may also be useful. Through a conversion function, the value of one of them can be obtained, for example, in another characteristic, always in read mode.

It is worth noting that to utilize the DAC, it is essential to activate the Serial Peripheral Interface (SPI) to establish proper communication between the microcontroller and the DAC. Activating the SPI involves configuring the corresponding pins on the microcontroller to serve as clock lines (SCK), input and output for data

(MOSI and MISO, respectively), and the slave select signal (SS). This process enables the microcontroller to send digital data to the DAC in a serial manner, facilitating the conversion of digital signals to analog. The accurate configuration of the SPI in the code is crucial to ensuring efficient and precise communication with the DAC.

Regarding the temperature, it can be obtained from the NTC pin of the LTC4125 [18]. To obtain this value, the pin is connected to one of the pins with analog-to-digital conversion function, to perform the conversion appropriately and obtain a comprehensible value. Once this is done, the temperature value can be introduced into a characteristic, also in read mode, to later collect the data and analyze it.Like previously with the DAC, to obtain the voltage value read from the NTC pin of the microcontroller (MCU), it is necessary to activate the Analog-to-Digital Converter (ADC) in the code. This will enable the MCU to read the analog signal from the NTC pin and convert it into a digital value. By establishing the appropriate resolution and reference, accurate voltage readings are ensured.

Taking these considerations into account, we can summarize the basic functions of our now peripheral TX as follows:

- Initialization of SPI and ADC ports
- Initialization of the DAC
- Reading and conversion of the temperature from the NTC pin
- Implementation of characteristics for the imposition, control, and reading of DAC parameters
- Implementation of a characteristic for reading the temperature of the TX

5.3.1 GATT profile

Once the objectives and measures to be taken are clear, we can proceed with the designation of the different characteristics. The table below specifies the new GATT profile of the TX in peripheral mode and the implemented characteristics for it:

Local Parameter Name	UUID	GATT Server Permissions	Description	Function
CHAR1	0xFFF1	Read / Write	Characteristic 1 Value	To order DAC to increase, decrease, or maintain the output voltages
CHAR2	0xFFF2	Read	Characteristic 2 Value	Old value imposed in CHAR1
CHAR3	0xFFF3	Read	Characteristic 3 Value	Temperature value
CHAR4	0xFFF4	Read / Notify	Characteristic 4 Value	Actual value imposed in CHAR1
CHAR5	0xFFF5	Authenticated Read	Characteristic 5 Value	PTHM value in mV

Table 5.1: GATT Server Characteristics

In the final appendix A, the implemented code for the TX in peripheral mode is showcased along with the changes made compared to its central version.

5.4 Final WPT System: The new Closed-Loop

In the detailed image below, we can observe our final WPT system with the migration of the TX to a peripheral role. As we can see, both the RX and the TX serve as peripheral components. To complete the loop, we utilize a Raspberry Pi in a central role, responsible for processing the data received from the RX and providing directives to the TX, which ultimately decides how to manage the transmitted power. Additionally, certain transmitter parameters, such as temperature and the DAC output value, are sent to the central device for further processing and result acquisition. This way, a new closed-loop WPT system is achieved, facilitating subsequent in-vivo tests, in addition to all the previously mentioned advantages.

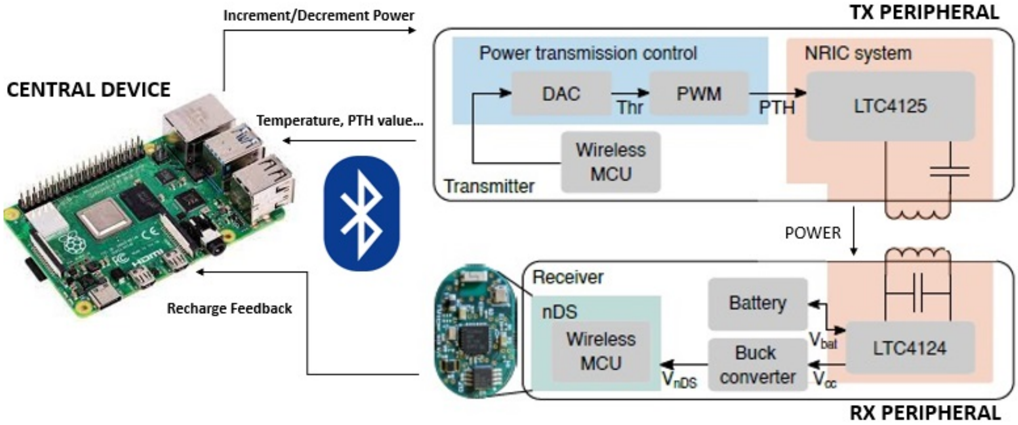

Figure 5.3: The new Close-Loop WPT system [7]

Chapter 6

Test and Results

To verify and confirm the proper functioning of the two designed transmitter versions, as well as their migration to a peripheral role and the implementation of an autonomous power system (including battery selection), various system configurations are proposed. This allows for a progressive verification of all blocks, ensuring they function correctly and meet the specified requirements.

In Figure 6.1, the complete system under test is depicted, including its connections and roles. Concerning the receiver, two different RX units were used for subsequent tests. On one hand, the Analog Instruments evaluation kit DC2770A was utilized, while on the other hand, the RX designed by [22] was employed, both based on the LTC4124 integrated circuit. The former uses a 17mm coil in its LC TANK, while the latter uses a 19mm coil. Both RX units serve different purposes: one demonstrates increased efficiency with the 19mm coil [22], and the other is used to verify its proper functioning. In our analysis, as depicted in the figure, we are solely interested in the receiver from the perspective of system integration, communication, and the TX's operation. Therefore, it is represented as a block in the scheme, along with nDS. Our focus will be on the breakdown of the TX and a block-by-block analysis of its components.

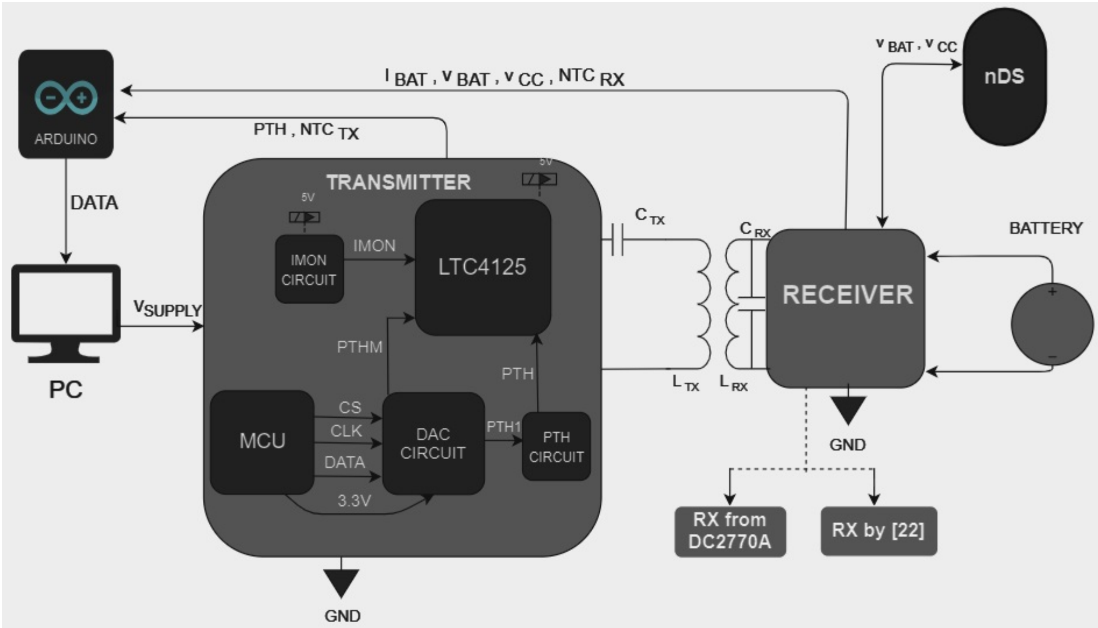

Figure 6.1: General System Under Test

6.1 Test Benches

Given that two different versions of the transmitter have been designed, it is crucial, as a first step, to verify the operation of the initial version. The functionality of the second version depends on the successful operation of the first. These versions were previously discussed in Chapter 3. In Figure 6.2, the connection of the TX system for data and parameter processing is illustrated. In this case, the transmitter is tested in central mode, focusing on making one change at a time. Thus, the analysis primarily assesses the proper functioning of the hardware, specifically the TX Board v1.0. From this illustration, two key points can be observed: data processing is carried out using Arduino and then processed in Matlab. For TX communication, the LAUNCHXL-CC2640R2F evaluation kit is still used, as the MCU integration occurs in the subsequent TX version.

Three critical characteristics for the proper functioning of the system are processed and analyzed: the TX temperature, the transmitted power efficiency, and, concerning the RX, the correct battery charging in terms of voltage, current, and charging time will be verified. This will be compared with previously conducted studies ([7], [21], [22]). Lastly, and notably important due to the system's packaging, the TX coil will be placed both beneath the TX board containing all the electronic circuits and on the side. The goal is to check if the coil's position relative to the TX's electronic circuit causes interference, potentially reducing the efficiency of the transmitted power.

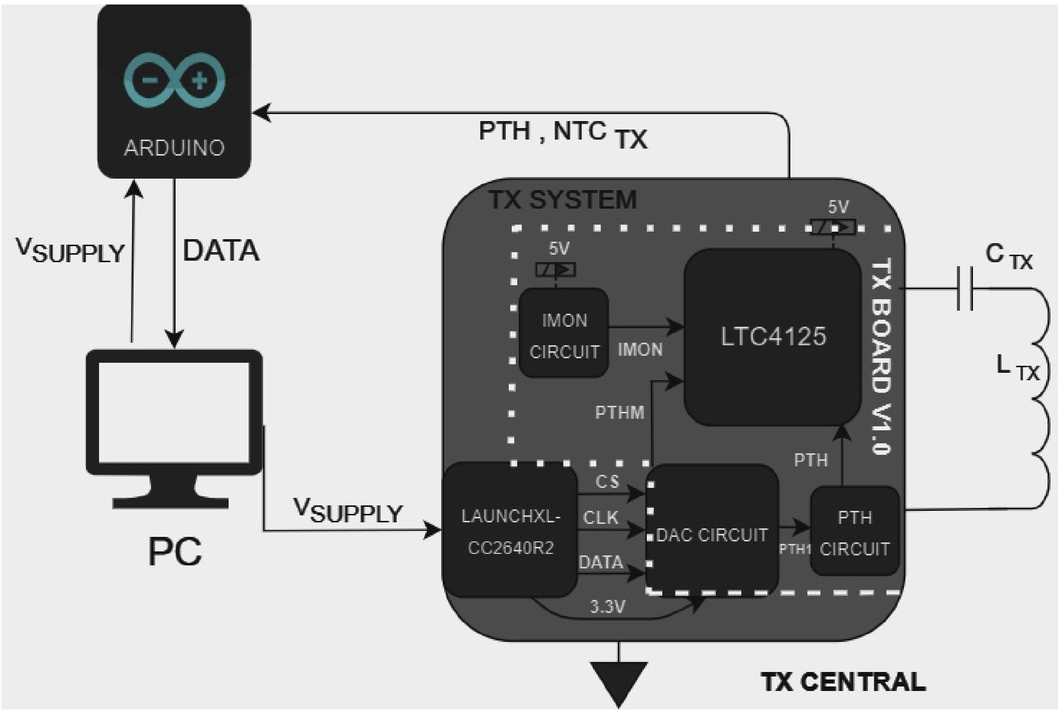

Figure 6.2: TX TEST BENCH v1.0

As observed in the Figure 6.2, in this initial test, we have:

- TX Board v1.0
- LAUNCHXL-CC2640R2F as the MCU for TX
- Arduino for data processing

In Figure 6.3, a more detailed representation of the blocks that make up the TX is shown for better understanding and analysis:

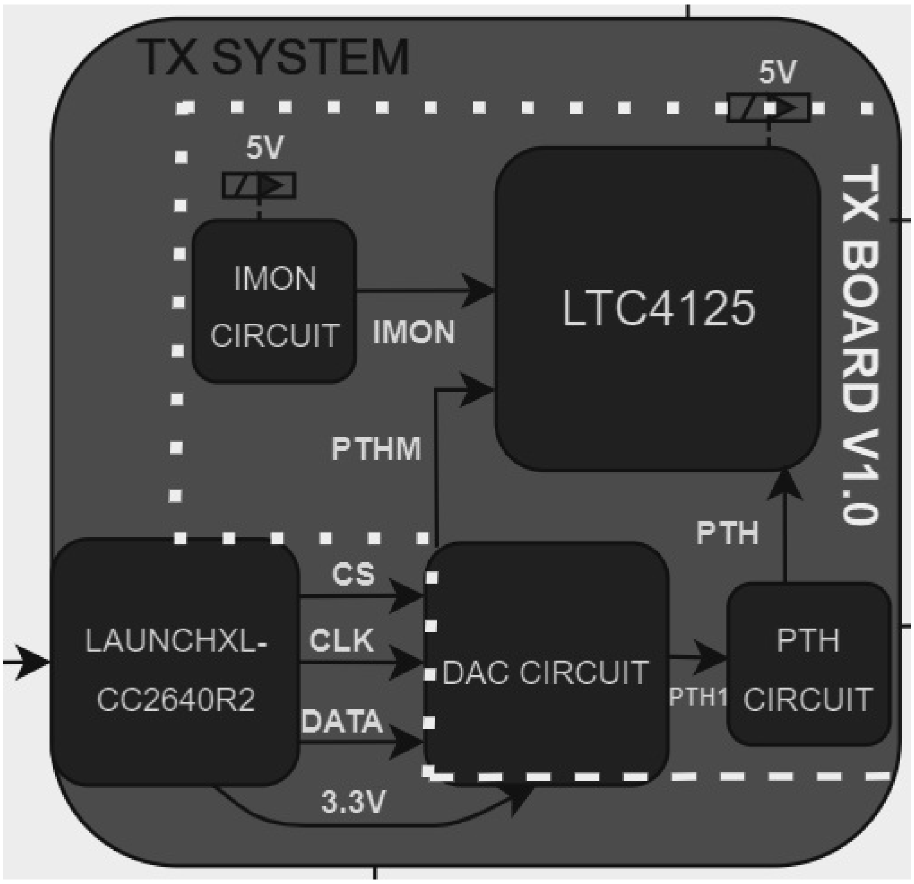

Figure 6.3: TX for Test Bench v1.0

In this case, the DAC circuit is powered anc configured via the SPI interface of the LAUNCHXL-CC2640R2F, while the TX board is powered directly from a power source. Arduino is employed for data processing obtained from TX during battery recharging. Below are the results obtained with this configuration: in the first case, the DC2770A evaluation kit and the 17mm coil were used. The coil was placed above the board. Lastly, another test was conducted with the RX designed by [22] and the 19mm coil, but this time positioned the coil above and below the board.

6.1.1 a) TX v1.0 with DC2770A as RX and the 17mm coil on the top

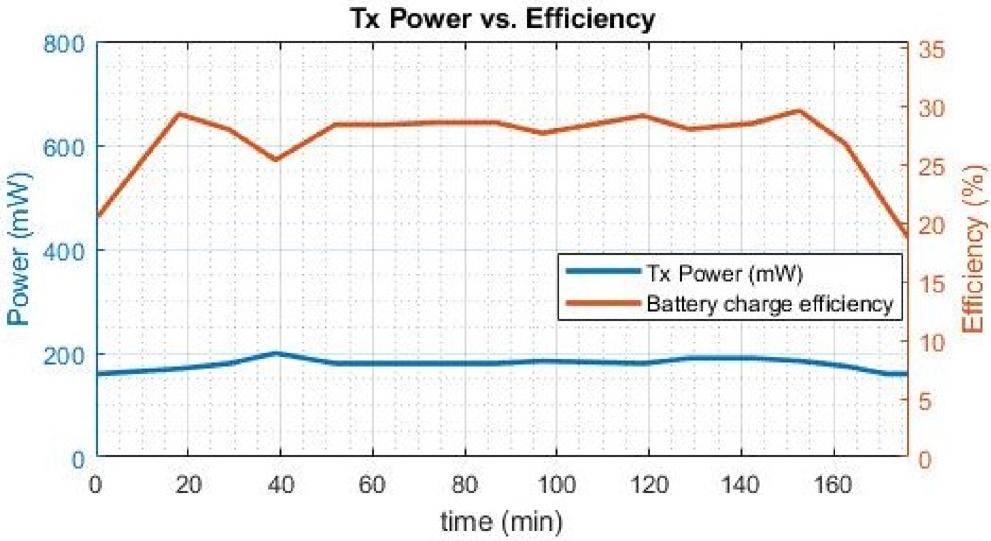

Figure 6.4: TX Power and Efficiency

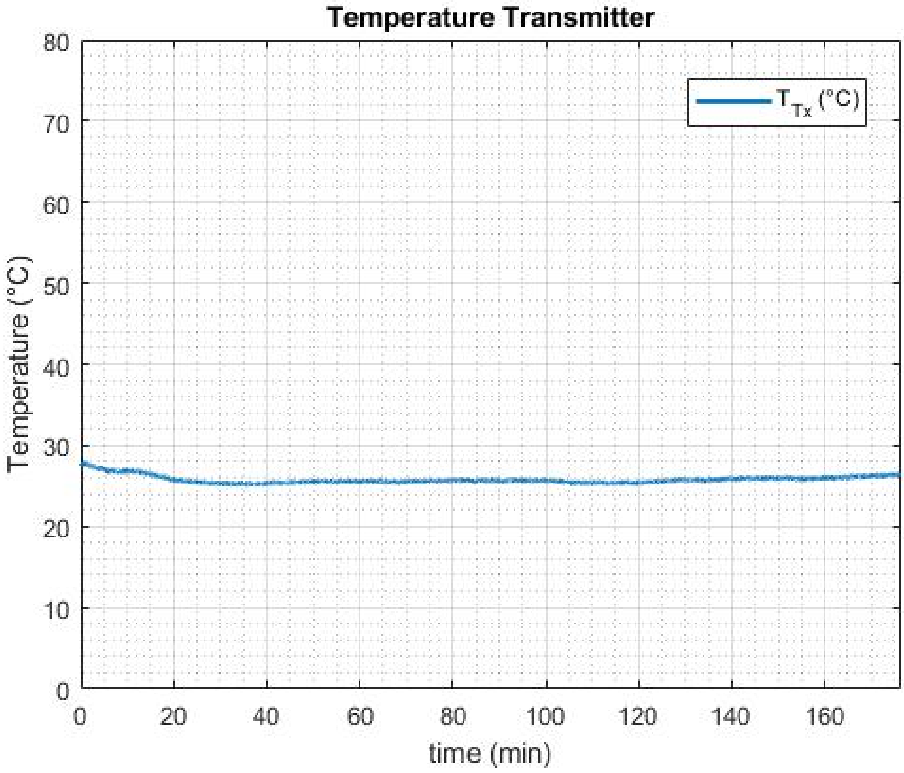

Figure 6.5: TX temperature

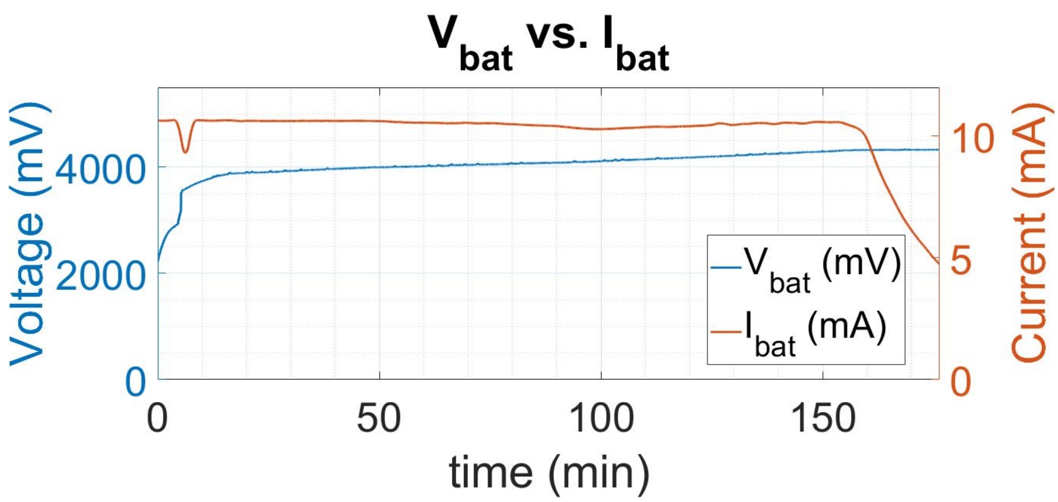

Figure 6.6: V_{bat} vs I_{bat}

6.1.2 b) TX v1.0 with RX designed by [22] and the 19mm coil on the top

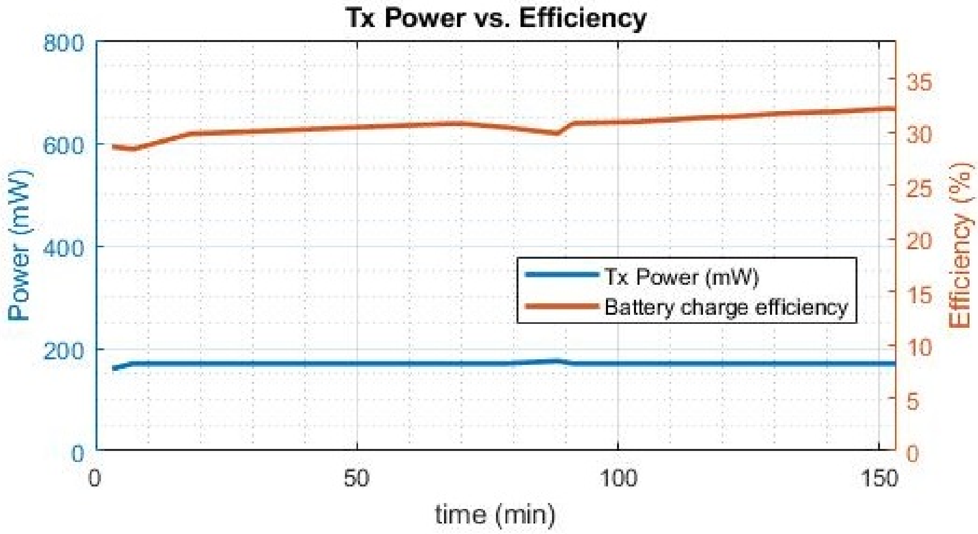

Figure 6.7: TX Power and Efficiency

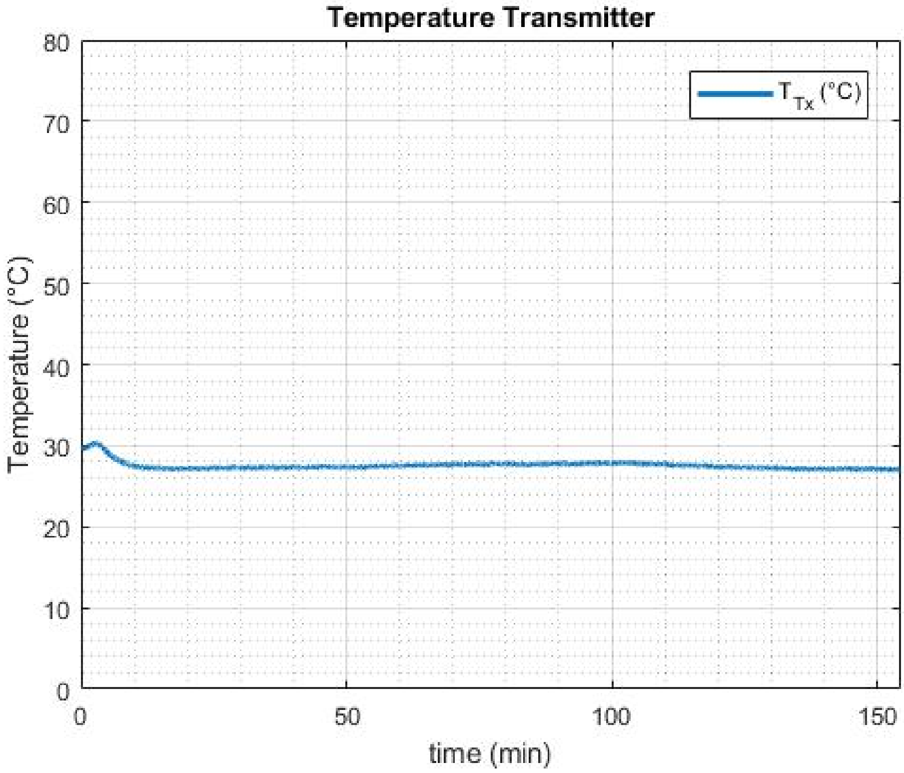

Figure 6.8: TX temperature

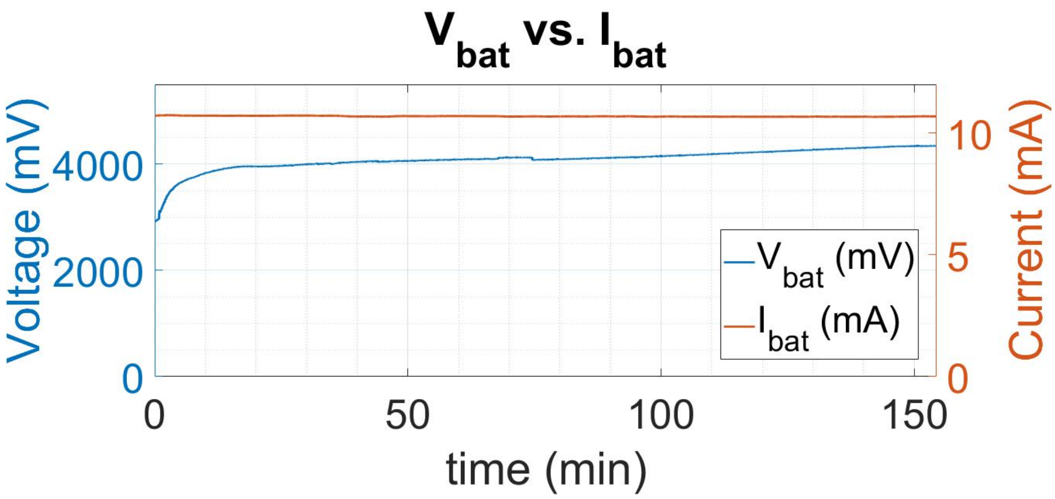

Figure 6.9: V_{bat} vs I_{bat}

6.1.3 c) TX v1.0 with RX designed by [22] and the 19mm coil on the bottom

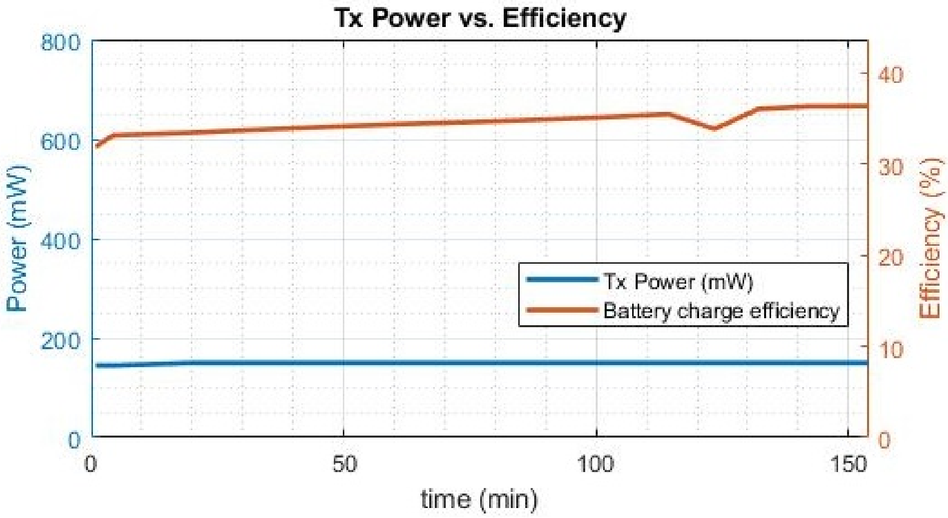

Figure 6.10: TX Power and Efficiency

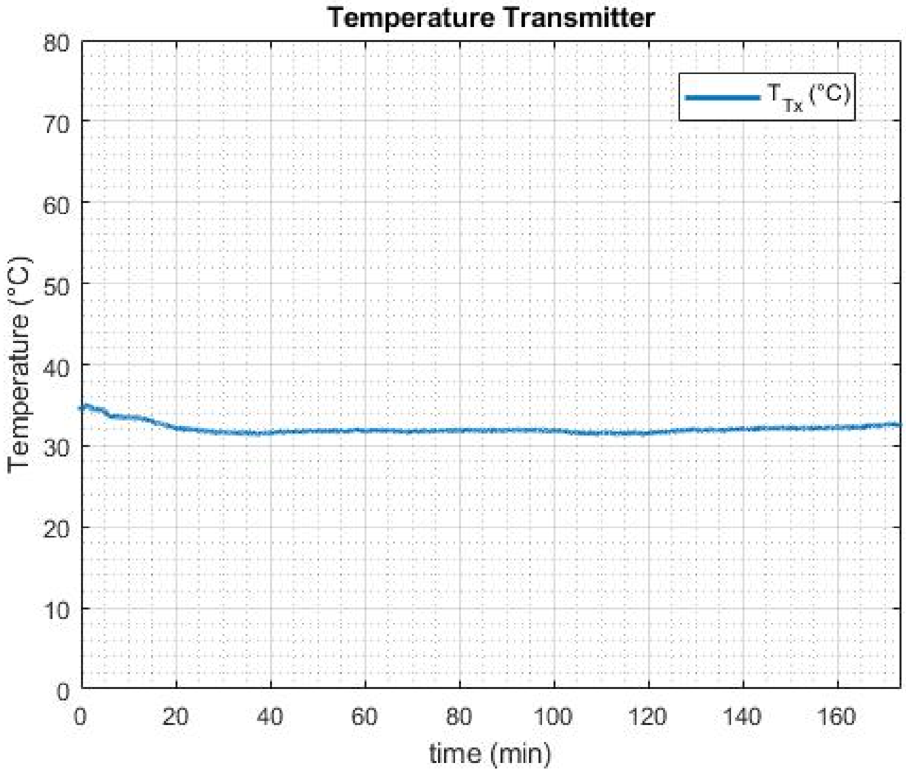

Figure 6.11: TX temperature

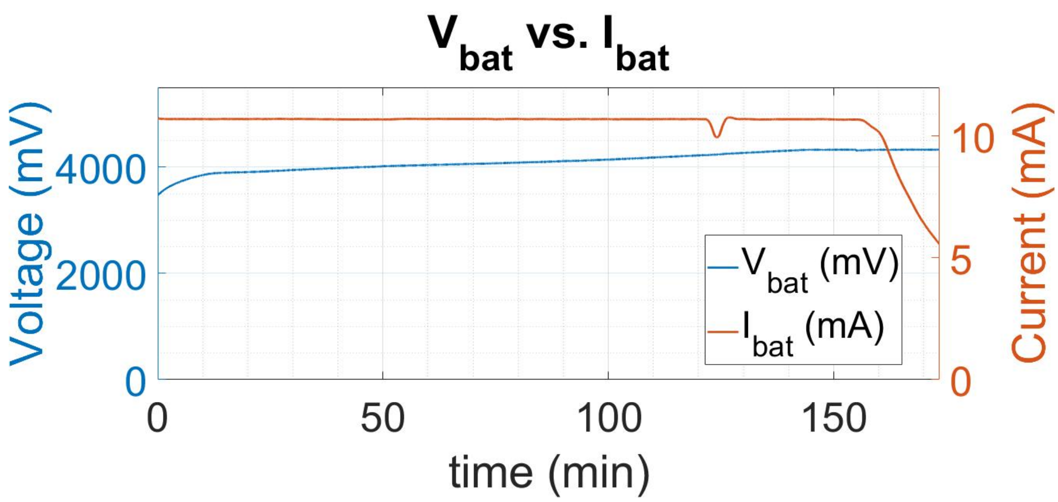

Figure 6.12: V_{bat} vs I_{bat}

Various conclusions can be drawn from observing Figures 6.4 - 6.12. Firstly, we note that the temperature of the TX is around 30°C in all three configurations. According to [18], these temperature values are acceptable for the correct operation of our transmitter, as they should not exceed 42°C. Regarding the efficiency of the transmitted power, in all three cases, it is above 30%, slightly higher when using a 19mm coil. These results are similar to those obtained in [7] and [22]. The highest efficiency values were obtained in the last case, with the use of the RX designed by [22] and the 19mm coil above our board. It is worth noting that the efficiency values may have decreased due to misalignment between the coils of the RX and TX and the connection cables for data collection. Finally, concerning the battery charging cycle, we observe that its current remains around 10 mA throughout the recharge process, reaching a battery voltage of 4.2 V in its CV phase after approximately 2.30 hours. These results align with those obtained in [7]. With these outcomes, we can affirm that the implemented hardware operates satisfactorily, achieving the expected results.

Secondly, having verified the optimal hardware performance, we proceed to implement a configuration to check the TX firmware's functionality. In this case, we close the loop between the RX and the TX through a device that will act as the central, while the TX and RX serve as peripherals. For practicality and convenience, and to avoid misalignments that could reduce the efficiency of transmitted power, a single test was conducted directly with the RX implemented in [22], and the coil was positioned above the board. The following figure illustrates the chosen configuration:

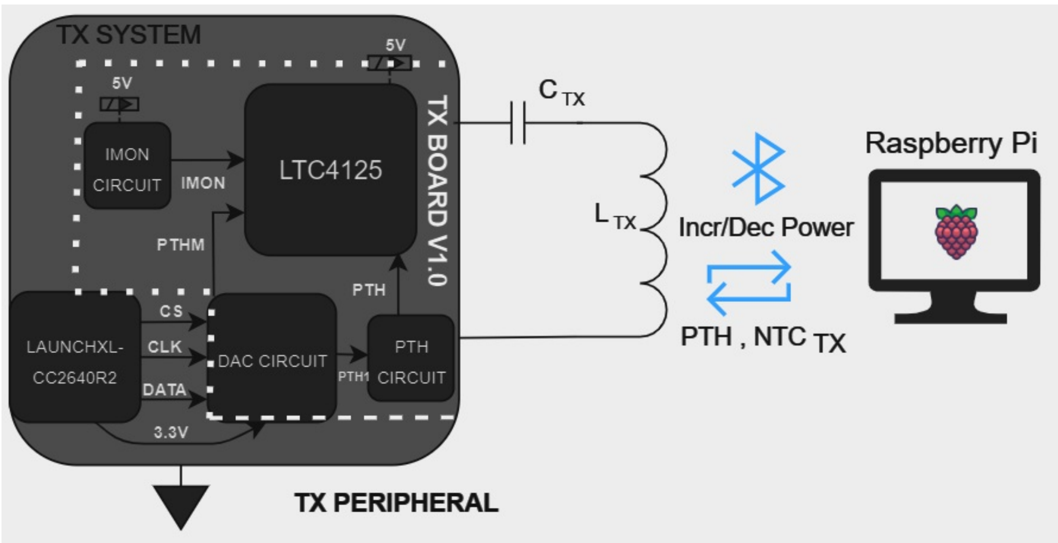

Figure 6.13: TEST BENCH v2.0

With respect to the blocks that make up the TX, the structure remains as previously shown in Figure 6.3. Then, as observed in Figure 6.13, in this test we have:

- TX Board v1.0
- LAUNCHXL-CC2640R2F as the MCU for TX
- Raspberry Pi for data processing

In the case of powering the different blocks of the system, the configuration from the previous test is maintained, as in this case, the evaluation aims to verify the firmware of the TX system.In this case, a qualitative analysis of the system was conducted, as opposed to the quantitative analysis performed earlier. This difference arises from the fact that in previous tests, data collection for subsequent analysis was carried out with Arduino. In this instance, obtaining various parameters from both the TX and RX is done using the Raspberry Pi. Currently, the Raspberry Pi is programmed to close the WPT loop, where data collection from the RX and TX is still in progress. For this reason, and to verify the proper functioning of the system, measurable parameters that are easy to obtain and provide reliable information about the system's operation were assessed.Using a multimeter, the battery voltage was measured over time to determine the charging cycle duration. Simultaneously, the transmitted power from the TX power source was measured, allowing for the calculation of system efficiency. After approximately 2.20 hours, the battery reached a stable voltage of around 4.2 V, indicating a fully charged state. Additionally, as illustrated in the figure below, the transmitted power maintained an average value of 150 mW, while the efficiency during the charging cycle hovered around 35%. These results demonstrate the successful migration of the TX to a peripheral role.

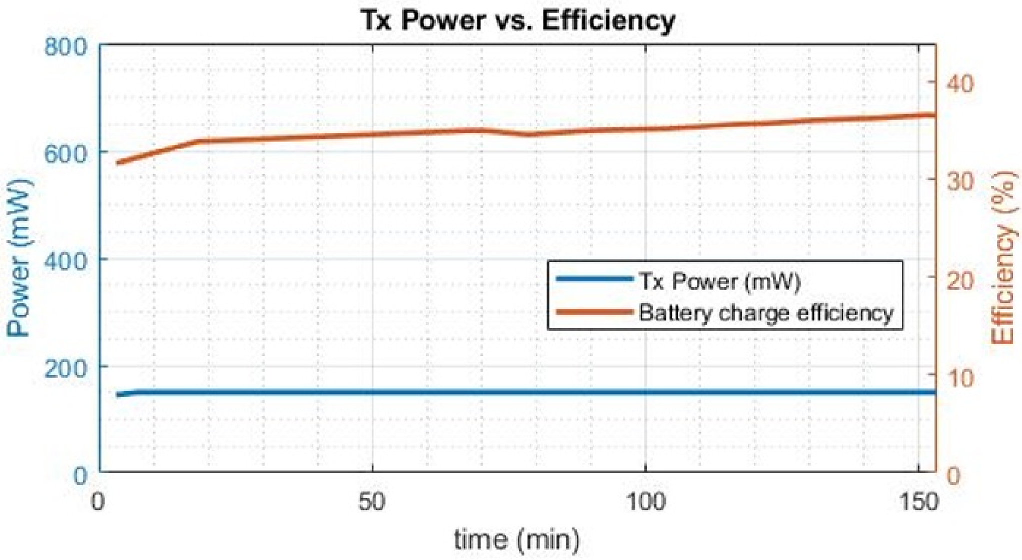

Figure 6.14: TX Power and Efficiency

Finally, a third test is proposed, but in this case, having verified the successful migration of the TX to a peripheral role, we choose to integrate the new hardware. As seen in Figure 6.15, the Self-Powering System (SPS) and the previously chosen battery from Chapter 4 are integrated first. With this change, we avoid the use of external power sources, as the system is now powered by the battery. Additionally, the second version of the TX, namely TX Board 2.0, is integrated, which, in broad terms, does not contain the DAC. Furthermore, nDS is utilized as a supporting device, implementing the necessary CC2640R2F MCU for communication between TX and the DAC. Consequently, we remove the LAUNCHXL-CC2640R2F from the TX system, thus achieving the final integration of the MCU. Ultimately, in this case, the TX is again used in peripheral mode for battery recharging.

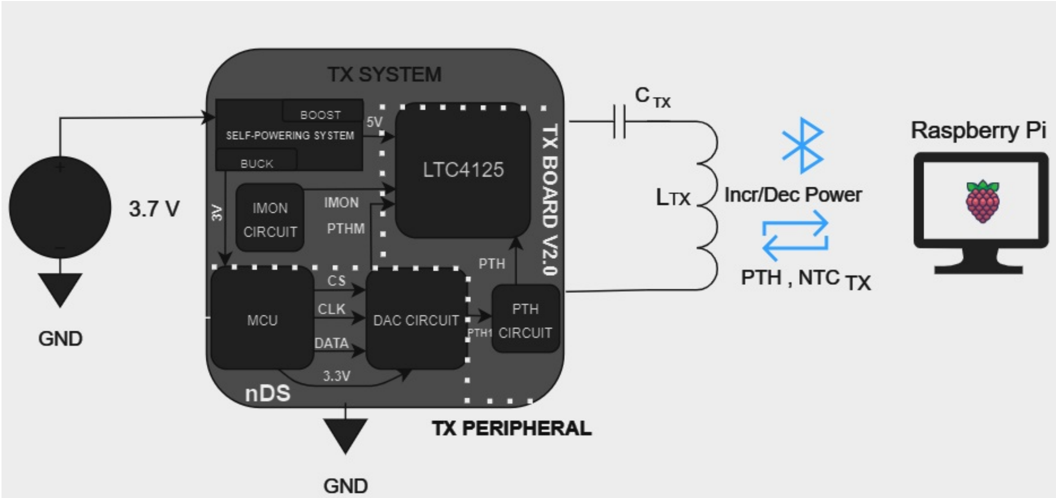

Figure 6.15: TEST BENCH v3.0

As observed in the figure above, in this test, we have:

- TX Board v2.0
- nDS containing: CC2640R2F as the MCU for TX and the DAC for the PTH Circuit
- Self-Powering System with its respective BOOST and BUCK converter circuits
- Battery to power the entire TX system
- Raspberry Pi for data processing

In Figure 6.16, a more detailed representation of the blocks that make up the TX is shown for better understanding:

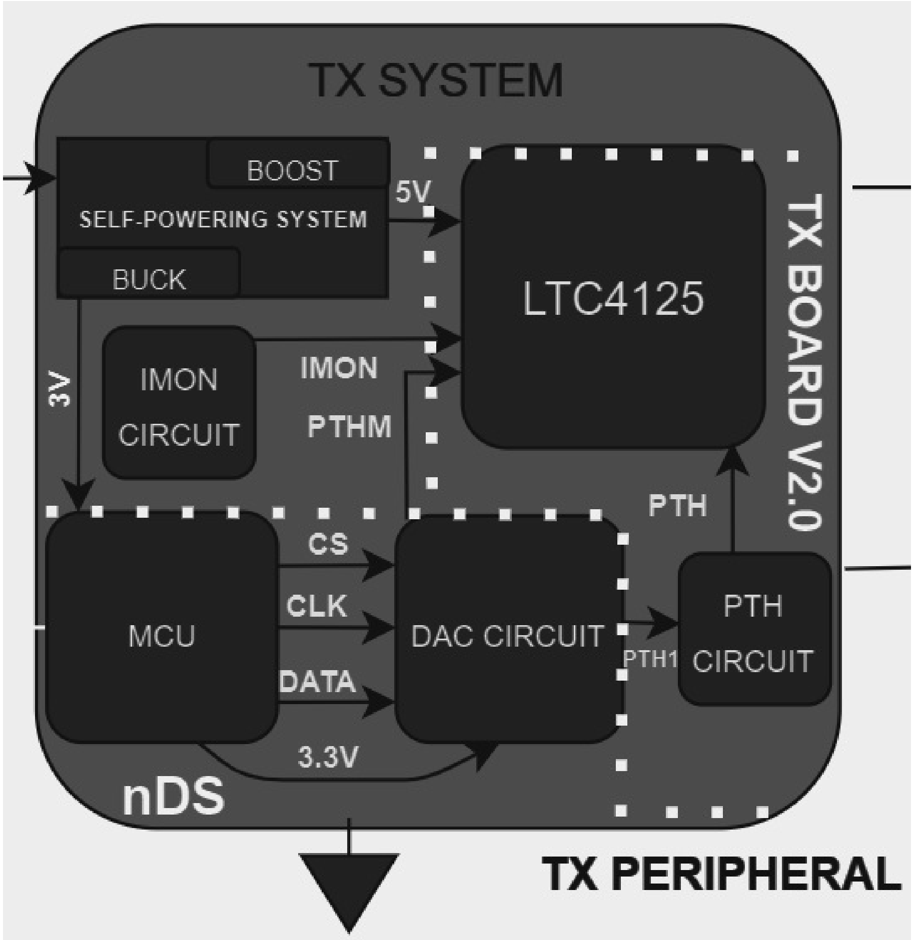

Figure 6.16: TX for Test Bench v3.0

Chapter 7

Conclusion and future perspectives

The main parameters and characteristics of the LTC4125 have been developed and explained to provide a more specific overview of the device we are working with. Different types of WPT were listed, emphasizing how, in the case of AIMDs, the use of the NRIC technique demonstrates superior capabilities compared to others. A precise discussion of the Bluetooth Low Energy (BLE) protocol was conducted, outlining its operation, features, and explaining its importance for our system, with a focus on the relevant characteristic functions. In this study, a closed-loop WPT system, previously designed and implemented in earlier studies, was considered. Various modifications were made to enable its use in in-vivo tests, ensuring IoT capability, and providing remote control and monitoring. The miniaturization of the TX was performed, involving the design and modification of various elements compared to previous versions. The MCU controlling its communication was integrated to encapsulate its various blocks into a single element, making it more compact and practical. An analysis of different batteries to power the TX was carried out, ultimately choosing a rechargeable battery meeting the system requirements in terms of voltage, current, and power. A battery charging board was selected, considering requirements such as dimensions and charging current. For the integration of the battery with our TX, an autonomous power system (SPS) was created, capable of supplying power to all its elements, from the LTC4125 to its MCU. A compact SPS was obtained, specifically designed to be connected to the TX, optimizing space during packaging. Regarding the firmware of the TX, specific work was done to migrate from the current central role to a peripheral role. Various BLE features were exploited to have absolute control over its parameters and thus control its transmitted power from a new central device. With this final modification, in-vivo tests of the entire system became possible. To verify the correct operation of all these modifications, various test configurations were put into play, yielding optimal results. However, several improvements can still be made. From the firmware perspective, BLE features can be further exploited for better management and control of the TX. For example, the EN pin of the LTC4125 can be configured to activate the device only during battery charging, reducing its power consumption. Another hardware modification could be the incorporation of an LED in the TX to indicate the optimal alignment of the TX and RX during a recharge cycle, improving the efficiency of transmitted power. Currently, there is no physical indication that this alignment is optimal during battery recharging. Moreover, the design of a device packaging all TX components has not been carried out. While all its blocks were chosen and designed to be packaged in the most efficient, practical, and compact way possible, careful consideration must still be given to designing the container, making the device more robust and portable.

Appendix A

In the following appendix, the primary lines of code implemented for **migrating the transmitter to its peripheral role** are presented. Various features are enumerated to ensure its proper functioning. The different functions that were involved are also displayed, along with a modification in the GATT profile of one of the features for potential use.

In these lines of code, we can see how the different functions are identified for calling, ranging from *Characteristics 1 to 5*.

```
static void SimplePeripheral_char2(uint8_t tempData); // vecchio value
static void SimplePeripheral_char3(uint8_t tempData); // temperature
static void SimplePeripheral_char4(uint8_t tempData); // new value
static void SimplePeripheral_char5(void); // notif of PTHM in mV
```

On the other hand, in the following lines of code, we can see how the **GATT profile** of **Characteristic 5** is modified, granting it reading permissions.

```
      // Characteristic Value 5
      {
        { ATT_BT_UUID_SIZE, simpleProfilechar5UUID },
        GATT_PERMIT_READ, // HT TO READ CHARACTERISTIC
        0,
        simpleProfileChar5
      },

      // Characteristic 5 User Description
      {
        { ATT_BT_UUID_SIZE, charUserDescUUID },
        GATT_PERMIT_READ,
        0,
        simpleProfileChar5UserDesp
      },
};
```

Next, the lines of code for the ***PerformPeriodicTask*** function are provided. In this function, we can observe the updating of values for Characteristics 3 and 4, which correspond to the temperature value and the last value set to the DAC in characteristic 1 from the device with the central role.

```
/*********************************************************************
 * @fn      SimplePeripheral_performPeriodicTask
 *
 * @brief   Perform a periodic application task. This function gets called
 *          every five seconds (SBP_PERIODIC_EVT_PERIOD).Here,
 *          the value of the first characteristic in the SimpleGATTProfile
 *          service is retrieved from the profile, and then copied into the
 *          value of the the fourth characteristic for the notifications.
 *
 * @param   None.
 *
 * @return  None.
 */
static void SimplePeripheral_performPeriodicTask(void)
{
  uint8_t valueToCopy;
  SimpleProfile_GetParameter(SIMPLEPROFILE_CHAR1, &valueToCopy);
  SimplePeripheral_char4(valueToCopy);
  // Start the ADC conversion
  ADC_convert(adc, &adcResult);
  SimplePeripheral_char3(adcResult);
```

In the following code snippet, we demonstrate how, within the ***processCharValueChangeEvt*** function, the previously implemented function from [7] is called to set a specific value in characteristic 1. This action is taken to modify the values of the DAC outputs for subsequent increases or decreases in transmitted power.The value of *Characteristic 5* is then updated with the new PTHM value.

```
/*********************************************************************
 * @fn      SimplePeripheral_processCharValueChangeEvt
 *
 * @brief   Process a pending Simple Profile characteristic value change
 *          event.
 *
 * @param   paramID - parameter ID of the value that was changed.
 *
 * @return  None.
 */
static void SimplePeripheral_processCharValueChangeEvt(uint8_t paramID)
{
  uint8_t newValue;
  switch(paramID)
  {
    case SIMPLEPROFILE_CHAR1:
      SimpleProfile_GetParameter(SIMPLEPROFILE_CHAR1, &newValue);
      FDBprocessNoti(newValue); // HT TO CHANGE THE VALUE OF THE OUTPUT OF THE DAC.
      break;

    case SIMPLEPROFILE_CHAR5:
    SimplePeripheral_char5();
       break;

    default:
      // should not reach here!
      break;
  }
}
```

In these lines of code, we observe how *Characteristics 2 and 3* update their parameters.

```
 * @fn      SimplePeripheral_char2
 *
 * @brief   This function gets called every time a new voltage change value is received
   from the central device.
 *          The value is read and then given as a BLE characteristic.
 */
static void SimplePeripheral_char2(uint8_t tempData)
{
    SimpleProfile_SetParameter(SIMPLEPROFILE_CHAR2, sizeof(uint8_t), &tempData);
}
/*********************************************************************
 * @fn      SimplePeripheral_char3
 *
 * @brief   Shows the value  of the temperature in Volts.
 *
 */
static void SimplePeripheral_char3(uint8_t tempData)
{
    SimpleProfile_SetParameter(SIMPLEPROFILE_CHAR3, sizeof(uint8_t), &tempData);
}
```

Finally, in these lines of code within *Characteristic 4*, we demonstrate how the value imposed on the DAC is notified (which can also be observed in *Characteristic 2* as it is in read mode). On the other hand, in *Characteristic 5*, we have the PTHM value in mV, made possible by converting its value using the ***uint16ToCharArray*** function.

```
/*********************************************************************
 * @fn      SimplePeripheral_char4
 *
 * @brief   This function notify  every time a new voltage change value is received from the central device.
 *
 */

static void SimplePeripheral_char4(uint8_t tempData)

{

    SimpleProfile_SetParameter(SIMPLEPROFILE_CHAR4, sizeof(uint8_t), &tempData);

}
/*********************************************************************
 * @fn      SimplePeripheral_char5
 * @brief   This function shows the value of PTHM in mV.
 */
static void SimplePeripheral_char5(void)

{

   char buffer[SIMPLEPROFILE_CHAR5_LEN];
   voltage=round(((Pthm_Val*3.3)/4095)*1000);
   uint16ToCharArray(voltage, buffer);
   SimpleProfile_SetParameter(SIMPLEPROFILE_CHAR5, SIMPLEPROFILE_CHAR5_LEN,buffer);
}
```

Bibliography

[1] Z. Zhang et al. “Wireless Power Transfer—An Overview”. In: *IEEE Transactions on Industrial Electronics* 66.2 (Feb. 2019), pp. 1044–1058. DOI: `10.1109/TIE.2018.2835378`.

[2] S.R. Khan et al. “Wireless Power Transfer Techniques for Implantable Medical Devices: A Review”. In: *Sensors* 20 (2020), p. 3487. DOI: `10.3390/s20123487`.

[3] L. Zhou et al. “Bluetooth Low Energy 4.0-based Communication Method for Implants”. In: *2017 10th International Congress on Image and Signal Processing, BioMedical Engineering and Informatics (CISP-BMEI)*. Shanghai, China, 2017, pp. 1–5. DOI: `10.1109/CISP-BMEI.2017.8302269`.

[4] Nicola Di Trani et al. “Remotely controlled nanofluidic implantable platform for tunable drug delivery”. In: *Lab on a Chip* 19 (June 2019). DOI: `10.1039/C9LC00394K`.

[5] Kateryna Bazaka and Mohan Jacob. “Implantable Devices: Issues and Challenges”. In: *Electronics* 2 (2012). DOI: `10.3390/electronics2010001`.

[6] Yeun-Ho Joung. “Development of Implantable Medical Devices: From an Engineering Perspective”. In: *Int Neurourol J* 17.3 (Sept. 2013). Epub 2013 Sep 30, pp. 98–106. DOI: `10.5213/inj.2013.17.3.98`.

[7] F. Del Bono et al. “Wireless Power Transfer Closed-Loop Control for Low-Power Active Implantable Medical Devices”. In: *2022 IEEE Sensors*. 2022, pp. 1–4. DOI: `10.1109/SENSORS52175.2022.9967268`.

[8] *RS Online Batteries*. `https://it.rs-online.com/web/p/batterie-a-bottone/1834290`. 2023.

[9] Michael Faraday. “Experimental Researches in Electricity”. In: *Philosophical Transactions of the Royal Society of London* 122 (1832), pp. 125–162. URL: `http://www.jstor.org/stable/107956`.

[10] G.R.M. Garratt. *The Early History of Radio: From Faraday to Marconi*. Institution of Engineering and Technology, June 1994, p. 93.

[11] J. Drews et al. “Primary batteries for implantable pacemakers and defibrillators”. In: *Journal of Power Sources* 97–98 (2001), pp. 747–749. ISSN: 0378-7753. DOI: 10.1016/S0378-7753(01)00649-8. URL: https://www.sciencedirect.com/science/article/pii/S0378775301006498.

[12] David C. Bock et al. “Batteries used to Power Implantable Biomedical Devices”. In: *Electrochimica Acta* 84 (2012), p. 10. DOI: 10.1016/j.electacta.2012.03.057.

[13] K. Agarwal et al. “Wireless Power Transfer Strategies for Implantable Bioelectronics”. In: *IEEE Reviews in Biomedical Engineering* 10 (2017), pp. 136–161. DOI: 10.1109/RBME.2017.2683520.

[14] C. Gomez, J. Oller, and J. Paradells. “Overview and Evaluation of Bluetooth Low Energy: An Emerging Low-Power Wireless Technology”. In: *Sensors* 12.9 (2012), pp. 11734–11753. DOI: 10.3390/s120911734. URL: https://www.mdpi.com/1424-8220/12/9/11734.

[15] Bluetooth. *The Bluetooth® Low Energy Primer*. Document Version: 1.1.0. Last updated: 17th January 2023. Bluetooth Special Interest Group. 2023. URL: https://www.bluetooth.com/wp-content/uploads/2022/05/The-Bluetooth-LE-Primer-V1.1.0.pdf.

[16] M. Afaneh. *Intro to Bluetooth Low Energy: The Easiest Way to Learn BLE*. Amazon Digital Services LLC - Kdp, 2018. ISBN: 9781790198153. URL: https://books.google.it/books?id=0UhjvwEACAAJ.

[17] Mindbowser. *Getting Started with BLE*. https://www.mindbowser.com/getting-started-with-ble/. 2023.

[18] Analog Devices. *Analog Devices LTC4125 Data Sheet*. https://www.analog.com/media/en/technical-documentation/data-sheets/4125f.pdf. 2023.

[19] Analog Devices. *Analog Devices DC2770A-B-KIT User Guide*. https://www.analog.com/media/en/technical-documentation/user-guides/DC2770A-B-KIT.pdf. 2023.

[20] *Mouser Datasheet*. https://www.mouser.it/datasheet/2/281/r44e-522712.pdf. 2023.

[21] Andrea Bontempi. “Wireless power transfer for implantable medical devices”. Mar. 2021. URL: http://webthesis.biblio.polito.it/17559/.

[22] Andrea Dentis. *Wireless Charging and Power Management System for Biomedical Implantable Devices*. 2023. URL: %5Curl%7Bhttp://webthesis.biblio.polito.it/id/eprint/27781%7D.

[23] Yeru Liang et al. "A review of rechargeable batteries for portable electronic devices". In: *InfoMat* 1.1 (2019), pp. 6–32. DOI: https://doi.org/10.1002/inf2.12000. eprint: https://onlinelibrary.wiley.com/doi/pdf/10.1002/inf2.12000. URL: https://onlinelibrary.wiley.com/doi/abs/10.1002/inf2.12000.

[24] Sony Energy Devices. *Sony Energy Devices - Keywords*. 2016. URL: https://web.archive.org/web/20160304224245/http://www.sonyenergy-devices.co.jp/en/keyword/.

[25] A. Arya and A. L. Sharma. "Polymer Electrolytes for Lithium Ion Batteries: A Critical Study". In: *Ionics* 23 (2017), pp. 497–540. DOI: 10.1007/s11581-016-1908-6. URL: https://doi.org/10.1007/s11581-016-1908-6.

[26] Weixiang Shen, Thanh Tu Vo, and A. Kapoor. "Charging Algorithms of Lithium-Ion Batteries: An Overview". In: *2012 7th IEEE Conference on Industrial Electronics and Applications (ICIEA)*. Singapore, 2012, pp. 1567–1572. DOI: 10.1109/ICIEA.2012.6360973.

[27] Weixiang Shen, Thanh Tu Vo, and A. Kapoor. "Charging Algorithms of Lithium-Ion Batteries: An Overview". In: *2012 7th IEEE Conference on Industrial Electronics and Applications (ICIEA)*. Singapore, 2012, pp. 1567–1572. DOI: 10.1109/ICIEA.2012.6360973.

[28] Edward K. F. Lee. "An active rectifier/regulator combo circuit for powering biomedical implants". In: *Proceedings of the IEEE 2013 Custom Integrated Circuits Conference* (2013), pp. 1–4. URL: https://api.semanticscholar.org/CorpusID:18069841.

[29] *CC2640R2F Datasheet*. Texas Instruments. 2023. URL: https://www.ti.com/lit/ds/symlink/cc2640r2f.pdf?ts=1700089546019%5C%26ref_url=https%5C%253A%5C%252F%5C%252Fwww.google.com%5C%252F.

[30] *P9-JT Thermistor Datasheet*. https://www.mouser.it/datasheet/2/362/P9-JT-Thermistor-1621687.pdf. 2023.

[31] *N-Channel Enhancement Mode Vertical DMOS FET Data Sheet*. https://ww1.microchip.com/downloads/en/DeviceDoc/TN0702-N-Channel-Enhancement-Mode-Vertical-DMOS-FET-Data-Sheet-20005941A.pdf. 2023.

[32] *NTR4501N Datasheet*. https://www.mouser.it/datasheet/2/308/1/NTR4501N_D-2319243.pdf. 2023.

[33] *760308101104 Datasheet*. https://www.we-online.com/components/products/datasheet/760308101104.pdf. 2023.

[34] *LTC4124 - Wireless Charging Receiver.* https://www.analog.com/media/en/technical-documentation/data-sheets/LTC4124.pdf. Analog Devices Data Sheet. 2023.

[35] *SR674361P Datasheet.* https://datasheetspdf.com/pdf-file/1414434/Mikroe/SR674361P/1. 2023.

[36] *DFR0208 Datasheet.* https://mm.digikey.com/Volume0/opasdata/d220001/medias/docus/2370/DFR0208_Web.pdf. 2023.

[37] *Adafruit Product 4410.* https://www.adafruit.com/product/4410. 2023.

[38] *TPS61023 Datasheet.* Texas Instruments. 2023. URL: https://www.ti.com/lit/ds/symlink/tps61023.pdf.

[39] *TPS82740B Datasheet.* Texas Instruments. 2023. URL: https://www.ti.com/lit/ds/symlink/tps82740b.pdf?ts=1700078676630&ref_url=https%253A%252F%252Fwww.ti.com%252Fproduct%252FTPS82740B.

[40] F. Del Bono et al. "Design of a Closed-Loop Wireless Power Transfer System for an Implantable Drug Delivery Device". In: *IEEE Sensors Journal* (2023). DOI: 10.1109/JSEN.2023.3270521.